Experimental methods and analysis of cold and dense dipolar exciton fluids

Experimental methods and analysis of cold and dense dipolar exciton fluids

Ronen Rapaport and Gang Chen

Bell Laboratories, Alcatel-Lucent, 600 Mountain Avenue, Murray Hill, NJ 07974, USA

Abstract

We review various aspects of our recent work on dipolar excitons in double quantum well systems. We describe and analyse different possible avenues for obtaining high density and cold dipolar exciton fluids that may enable an observation of quantum phase transitions in excitonic systems. These avenues include free dipolar exciton fluids, dipolar exciton fluids in electrostatic traps and in excitonic rings. We present our experimental and modelling work on the exciton dynamics in such systems, and discuss our current view of the advances made and the challenges that remain in this fast evolving and promising field of research.

(Some figures in this article are in colour only in the electronic version)

1. Introduction

The search for the elusive quantum phase transitions of excitons in semiconductors has a long and interesting history stretching back about half a century. As relatively 'new comers' to this rich and lively research field, we do not intend to give here a comprehensive review of the results that have been collected over the years by the many research groups that were and are working in this field. Instead, we will try to give a brief summary of our own research efforts, in the broader context of the general advancements and the exciting and intriguing new results that emerge in a fast growing rate in recent years, mostly those from long lived indirect excitons, also known as dipolar excitons, in high quality GaAs double quantum wells (DQW's) grown by molecular beam epitaxy. We will try to convey what is our current understanding of the dynamics of such exciton fluids under different experimental situations, what seem to be the main obstacles, and what are the emerging promising techniques that could overcome (and already do to some extent) those obstacles and enable the long sought observation and unambiguous identification of new thermodynamic phases of exciton fluids.

2. Background

Two dimensional (2D) excitons, which are Coulomb bound electron–hole pairs (quasi-particles) confined in a semiconductor quantum well (QW) layer can be considered as bosons,

as long as their density is low enough such that the identity of their fermionic constituents is essentially hidden within the excitonic atomic-like structure. This will happen when the average inter-exciton distance is much larger than the size of the exciton, or its Bohr radius. Therefore, under the right conditions, excitons are expected to undergo quantum phase transitions, the exact nature of which will depend on the interplay between their Bose–Einstein statistics and their mutual interactions. Such a transition could be, for example, to a Bose–Einstein condensate [1] somehow similar to trapped alkali atoms [2], or to a condensed superfluid state [3–5], resembling, for instance, superfluid ^{4}He. Furthermore, due to the very small effective mass of excitons compared to atoms, these quantum phase transitions are expected at temperatures of the order of one to few kelvins, which are achievable with a standard liquid He cryogenic equipment commonly available in many laboratories. A major disadvantage of excitons compared to real atoms, however, is that they need to be (usually optically) excited and that they live in the material for only a very short lifetime afterwards. Optically exciting excitons means that their initial state is not in thermal equilibrium and that right after their excitation they are hotter than their semiconductor host material. Excitons in single QW's, for example, have radiative lifetimes which are typically in the sub-nanosecond range, after which the exciton's electron and hole will spontaneously recombine by emitting a photon. This limits the time available for these excitons to cool down to the host lattice temperature and achieve thermal equilibrium, and seems to be a major obstacle for achieving cold and well thermalized exciton fluids. Another obstacle for excitons is that they tend to agglomerate to drops of electron–hole plasma when they become dense enough so that their effective attractive interaction becomes important. This limits the useful exciton densities one can work with, making it hard to achieve densities high enough for quantum correlations and quantum statistical degeneracy to take place with achievable crystal temperatures and without agglomeration. Thus, a clear observation of these elusive phase transitions remained one of the toughest challenges that researchers in the exciton physics field have been working toward for the past several decades. As mentioned earlier, we would not attempt to describe all that previous work, and one can refer to some recent reviews [6, 7] and the references within for a better and fuller perspective of the scope of this field. In the rest of this paper, we will discuss a unique class of QW excitons, that are spatially indirect, that have been introduced to this field of study in the last decade or so, and that we have been working on for the last few years. In these spatially indirect exciton systems, the constituent electrons and holes of the lowest energy levels are separated into two weakly coupled QW's with an inter-well energy barrier [8, 9] and an external bias, as is illustrated in figure 1. This separation results in two unique features. First, since the electron and the hole are in two different QW's, separated by a high energy barrier, the overlap of their wavefunctions is dramatically reduced, hence the exciton lifetime can become extremely long (in the microseconds regime) and in principle should easily accommodate for the necessary cooling and thermalization processes, an important improvement over excitons in single QW's. Luckily, the exciton binding energy is much less dramatically reduced, as the direct term of the Coulomb interaction does not depend on this overlap [10, 11]. Secondly, the indirect excitons are intrinsically dipolar, as the electron and hole are separated in different spatial positions along the growth direction, resulting in a permanent (within the exciton lifetime of course) electric dipole moment. The excitons dipole moments are *all* aligned perpendicular to the QW plane, resulting in a net dipole–dipole repulsive interaction between them. This short range interaction prevents the unwanted exciton agglomeration and is expected to play a crucial role in the physics of quantum phase transitions of such an exciton fluid, which is a good model system for interacting bosons in two dimensions.

All of this makes the dipolar exciton system a very promising and interesting system to explore, and it might seem that just by shifting from direct excitons in single QW's to dipolar
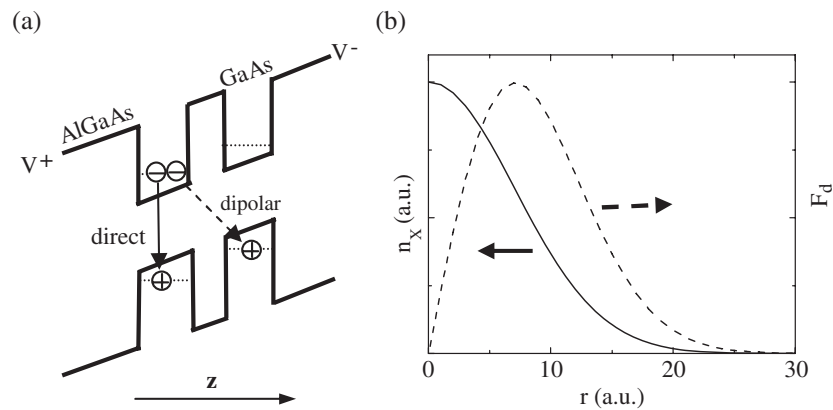
Figure 1. (a) Band diagram for GaAs/AlGaAs DQW structure under external bias and the formation of dipolar excitons. (b) A Gaussian radial density profile of a dipolar exciton fluid and the internal repulsion force due to the dipole interaction.

excitons in DQW's, all problems are solved and observing quantum phase transitions is now straightforward. Unfortunately, this is quite far from being true. Here we will try to portray our current view of what are at least some of the remaining problems with the dipolar exciton systems and discuss some of the techniques that have recently evolved to overcome these remaining challenges. These techniques are being experimentally tested currently, providing results which suggest that, being quite cautious, some very interesting things occur with these exciton systems at high densities and low temperatures.

3. Overview

The structure of the paper is as follows: in section 4, we present the model that describes the density and temperature dynamics of dipolar excitons. This model will be used throughout the paper to analyse and compare with experimental results. In section 5 we describe the dynamics of free expanding exciton fluids under laterally homogeneous bias and discuss the consequences of the dipolar repulsion and expansion on the density and temperature evolution of the exciton fluid. In section 6, we propose and experimentally realize electrostatic exciton traps which prevent the excitons from expanding and therefore eliminate some of the disadvantages of a free expanding exciton fluid in achieving high density and cold excitons. Measurements and model analysis show that a high density dipolar exciton fluid can indeed be confined within the trap for a long time and it may have reached quantum degeneracy. In section 7, we discuss modelling and experiments on exciton ring systems, where an in-plane charge separation may provide a source for obtaining cold excitons far away from the excitation source. In section 8, we summarize issues related to the exciton cooling in the various experimental geometries, i.e., free expanding excitons, trapped excitons, and exciton rings, and discuss the pros and cons of pulsed as well as continuous wave (CW) optical excitations. Finally, in section 9, we briefly analyse the stability of dipolar exciton crystal phase in a confined geometry as a possible competitor for exciton quantum phase transitions. In section 10 we summarize the main points of this paper and refer to new experimental results that may suggest exciton quantum correlations.

4. Dipolar exciton dynamics model

In this section we present a simple model for the dynamics of dipolar excitons [12–14]. It is a good starting point to understand some of the particular properties of dipolar excitons and their effect on the density and temperature evolution of the excitons. This model will be used in later sections to analyse experimental results of free expanding dipolar excitons, excitons in traps, and dipolar exciton rings.

Consider the DQW structure under an external electric bias as is illustrated in figure 1(a). There are two distinct excitations, a direct exciton, where the electron and the hole are in the same QW, and the dipolar exciton, in which the electron and the hole are in two different QW's. Under large enough applied bias, the dipolar exciton has a lower transition energy than the direct exciton, and its red-shifted energy (with respect to the direct exciton transition) is bias dependent.

A distribution of such dipolar excitons can be optically excited in the plane of this structure, resulting in an in-plane density profile of dipolar excitons, $n_X(\vec{r}, t)$ (here $\vec{r} \equiv \vec{r}_{||}$ is the in-plane spatial coordinate). Due to the separation of electrons and holes into two different planes along the growth direction, the resulting excitons carry a permanent dipole moment pointing perpendicular to the QW planes. As all the dipoles of the excitons are aligned in the same direction, there is a net repulsive dipole–dipole interaction between the excitons. In the mean field approximation, neglecting exciton–exciton correlations, this repulsion leads to an extra interaction energy term per exciton, which is linear with the local exciton density [15, 16, 12]:

$$\varepsilon_d(\vec{r}) = \frac{4\pi e d}{\epsilon} n_X(\vec{r}) \equiv \alpha n_X(\vec{r}), \tag{1}$$

where d is the exciton dipole, and ϵ is the background dielectric constant. The resulting effective dipole repulsion force,

$$\mathbf{F}_d(\vec{r}) = -\alpha \nabla n_X, \tag{2}$$

is proportional to the density gradient. Figure 1(b) shows the force profile for a radial Gaussian distributed exciton fluid.

To describe the dynamics of such a collection of excitons, some assumptions on the forces and scattering processes of the excitons are made. There are three relevant scattering mechanisms which are considered here. The first one is the fast, density dependent exciton–exciton scattering [15], which is dominant at high exciton densities. Such a scattering process, with a characteristic time much shorter than any other timescale of the dynamics, yields an internal exciton equilibrium and therefore a well defined exciton temperature, T_X. It also yields a temperature and density dependent diffusion coefficient, $D_{XX} = D_{XX}(n_X, T_X)$. The derivation of D_{XX} which is used in this model, was done by Ivanov *et al* in [12], where we refer the readers for all the relevant details. The other mechanism is due to scattering of excitons with the QW disorder, which is density independent but yields a diffusion coefficient, $D_{do} = D_{do}(T_X)$, which depends on the QW width to the sixth power (see [17, 13] for a more detailed description). Those two scattering processes yield an effective diffusion of excitons, which includes both the exciton–exciton and disorder contributions. The combined effect can be included in an effective diffusion coefficient, $D(n_X, T_X)$, given by: $D = D_{XX} D_{do}/(D_{XX} + D_{do})$ which is density and temperature dependent. At high exciton densities, exciton–exciton scattering is dominant and $D \to D_{XX}$ while at the low density limit the dominant scattering mechanism is QW disorder and thus at that limit, $D \to D_{do}$. The third scattering process that is responsible for the exciton–lattice thermalization is the exciton–phonon scattering, which is the slowest process at low temperatures. We use T_l to denote the lattice temperature. In a simplified picture, we model this thermalization with a single characteristic time (τ_l).

Under either internal or external forces, the resulting exciton currents are related to the various forces through the exciton mobility as: $\mathbf{J} = n_X \mu \mathbf{F}$. The exciton mobility, μ, is in turn related to the effective exciton diffusion coefficient, D, through Einstein relations for a Bose–Einstein gas in the non-interacting limit in two dimensions: $\mu = (D/kT_0)(e^{T_0/T_X} - 1)$ [12]. Here $T_0 = (2\pi\hbar^2 n_X)/(kgm_X)$ is the degeneracy temperature, $m_X \cong 0.2\, m_e$ is the exciton mass, and $g = 4$ is the exciton spin degeneracy in typical GaAs QW structures. Three force terms are included in this model, leading to three expressions for the exciton currents:

(i) The dipole repulsion force $\mathbf{F}_d = -\alpha \nabla n_X$, which is taken from equation (2), and is a consequence of the dipole–dipole interaction. The corresponding current term is

$$\mathbf{J}_d = -\mu\alpha n_X \nabla n_X. \tag{3}$$

(ii) The diffusive force, due to the gradient of the chemical potential, given by $\mathbf{F}_D = -\nabla\zeta = -\frac{kT_0/n_X}{e^{T_0/T_X}-1}\nabla n_X$, where $\zeta = kT_X \ln(1 - e^{-T_0/T_X})$ is the chemical potential in the non-interacting limit. This yields a current term of the form:

$$\mathbf{J}_D = -D\nabla n_X. \tag{4}$$

(iii) External forces, represented by $\mathbf{F}_{\text{ext}}$, leading to a current term:

$$\mathbf{J}_{\text{ext}} = n_X \mu \mathbf{F}_{\text{ext}}. \tag{5}$$

The dynamics of a dipolar exciton fluid can then be described by two coupled equations for the exciton fluid density and temperature. The time evolution of the exciton fluid density is described by the following diffusion equation:

$$\frac{\partial n_X}{\partial t} + \nabla \cdot (\mathbf{J}_D + \mathbf{J}_d + \mathbf{J}_{\text{ext}}) + \frac{n_X}{\tau_X(\vec{r})} - I_X(r, t) = 0. \tag{6}$$

Here, $I_X(r, t)$ is the exciton generation source, $\tau_X(\vec{r})$ is the lifetime of the excitons, which is assumed, for simplicity, to be density independent but can, in general, depend on position, as in the case of exciton traps to be discussed later on.

The second equation describes the time evolution of the exciton fluid temperature, T_X [14, 18]:

$$\frac{dT_X}{dt} = -\left[\frac{1}{kN_X}\left(\frac{\partial E_d}{\partial t}\right)_{N_X} + \frac{T_X - T_l}{\tau_l}\right] + I_T, \tag{7}$$

where E_d, the total potential energy due to the dipole–dipole interactions is given by: $E_d = \int \alpha n_X^2(\mathbf{r}, t)\mathrm{d}^2 r$ and $N_X(t) = \int n_X(\mathbf{r}, t)\mathrm{d}^2 r$ is the total number of dipolar excitons. The first term on the RHS of equation (7) represents the heating of the exciton fluid due to the driven expansion: as dipolar excitons expand and their density drops, the potential energy stored due to their mutual repulsive interaction is released in the form of kinetic energy, which through the fast exciton–exciton scattering is transformed to heat. The second term represents the thermalization of the excitons with the lattice, and the last term, I_T represents all other heating terms, such as external heating by optical pumping, hot carriers, etc. This term can be absent for pulsed excitation after the optical pulse is turned off but can be quite complicated in general and we will discuss the importance of external heating sources toward the end of this paper, in section 8.

Equations (6) and (7) are coupled and can be numerically evaluated. In the following sections we will use the model as a tool to analyse experimental results under different conditions, and to get more insight into the underlying dynamical processes.
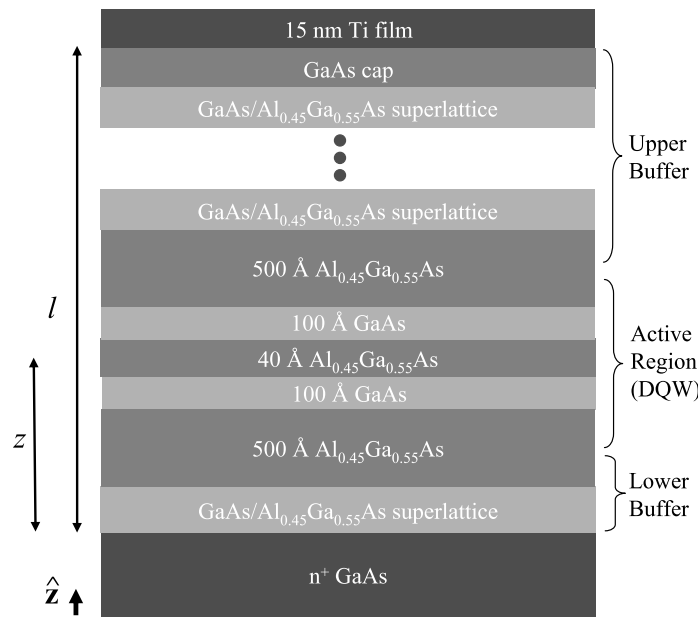
Figure 2. A typical design of a GaAs DQW sample structure.

5. Free expanding excitons

The simplest and most straightforward way to create a high density dipolar exciton fluid is to optically excite carriers in a homogeneously biased sample. This excitation, usually not resonant with the dipolar exciton transition (resonant excitation is very inefficient due to the very low absorption coefficient of the dipolar exciton transition), results in non-thermalized, hot charged carriers. After a short excitation pulse, carriers with opposite signs that remain in the same QW will quickly recombine through the direct exciton transition channel (with typical times of tens of picoseconds). However, due to the energy profile of the biased QW, there will be a strong tendency of electrons and holes to accumulate in different QW's, resulting in a build-up of a dipolar exciton population. This section describes both experimental measurements and theoretical modelling of the dynamics of the dipolar excitons that are free to move in the QW plane. The main finding is that the strong dipolar pressure always dominates the driving forces for the exciton motion at densities relevant to exciton quantum degeneracy. This pressure leads to a fast spatial expansion of the excitons, reducing the exciton density below the critical value for quantum degeneracy much faster than the exciton recombination lifetime [13]. In the mean time, the dipole repulsion also acts as a significant heating source which converts repulsion potential energy into thermal energy during the expansion via exciton–exciton scattering [14, 18].

5.1. Experimental results

The DQW sample structure studied in our experiments is illustrated in figure 2. The QW's are 100 Å thick and are separated by a 40 Å $Al_{0.45}Ga_{0.55}As$ barriers. Two buffer zones are grown below and above the QW structure. They consist of narrow QW superlattice structures. The superlattice structures are designed to capture charged carriers travelling through the sample
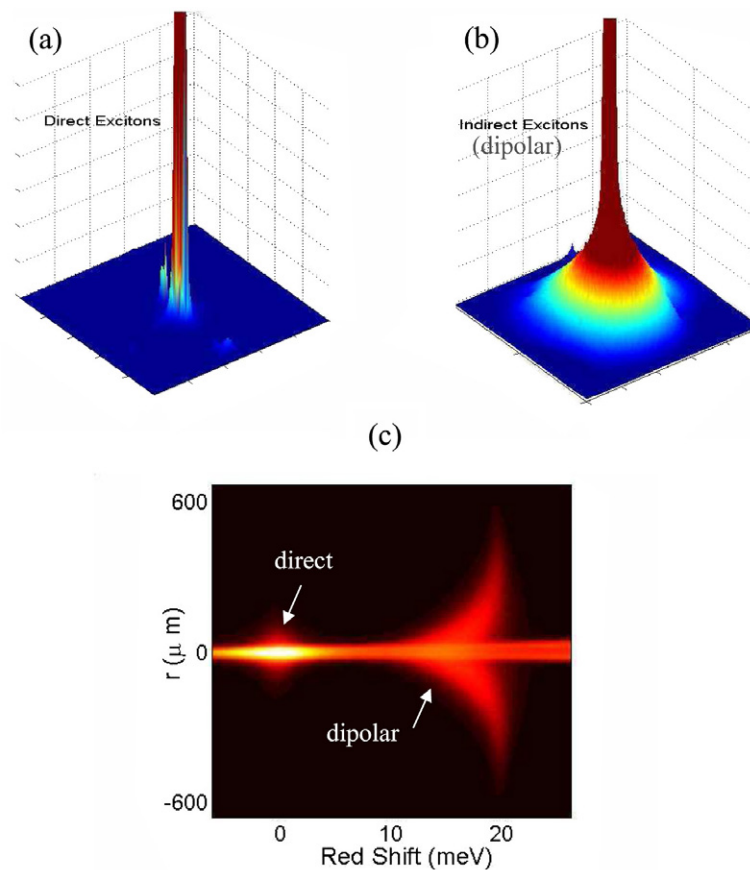
Figure 3. The emission image taken from the (a) direct and (b) dipolar excitons. The images are 1×1 mm^2 in size. The large spike in the centre is the residual direct exciton emission not completely rejected by the filters. (c) Spectral image of the direct and dipolar excitons. All images are taken with a CW He–Ne laser excitation (see text).

and thus reduce the dark currents. Under bias voltages of a few volts the dark current density is measured to be smaller than 1 μA cm^{-2}. The sample thickness, from the bottom to the top electrode, is denoted by l. The DQW plane is perpendicular to the growth direction ($\hat{z}$) and its vertical position in the sample is given by z, measured from the bottom electrode. The importance of the parameter z/l will be discussed later when we implement electrostatic traps for dipolar excitons. A small z/l is achieved by growing a much thicker upper buffer than the lower one. The structure is grown on an n^+ GaAs substrate, which also serves as the bottom contact. A semitransparent metallic (titanium) film with thickness of ∼15 nm was evaporated on top of the sample as the top contact. For the study of free exciton expansion, the titanium contact is extended to the entire sample and therefore the DQW is homogeneously biased. The optical transmission through the film in the near IR is roughly 15% and is enough for optical excitation of excitons and collection of emission.

The consequence of the free expansion of excitons driven by various force terms is clearly seen by the measurement of figures 3(a) and (b), in which the emission images of the direct and dipolar excitons are taken using narrow spectral bandpass filters tuned to their corresponding optical transition energies. The excitons are excited by a CW He–Ne laser beam of 4.7 mW

focused to 40 μm. The sample is biased at 1.5 V. We see that while the direct exciton emission is observed from an area determined by the excitation spot, the dipolar exciton fluid is dramatically larger and can extend to hundreds of microns in diameter. Figure 3(c) shows the spectral image of the direct and dipolar excitons. The exciton emission is spatially and spectrally resolved in the vertical and horizontal directions, respectively. We see that as the dipolar excitons expand to a large fluid and their distance from the excitation spot increases, their spectrum shifts to red. This is a consequence of a decreasing density (the relation between exciton density and emission energy will be discussed in more details later in section 6).

The time evolution of the exciton fluid after a short pulse excitation was studied experimentally by Vörös *et al* [17] by time resolving the dipolar exciton spatial emission profile after a non-resonant, focused, short pulse excitation on a biased sample similar in design to the one shown in figure 2. The main results are shown in figure 4(a) for a 100/40/100 Å DQW sample (for more details on the sample structure and the experiments performed, see [17]). Figure 4(b) plots the square of the width (σ^2) of the dipolar exciton emission profile as a function of time for samples with various QW widths. It shows the fast expansion of the exciton fluid within a short time of only few tens of nanoseconds. We will show later that this is a result of the strong dipolar repulsion between excitons (the second term of equation (6)). At later times, as the exciton density (and consequently the exciton density gradient) decreases, the expansion becomes diffusive (dominated by the first term of equation (6)), which is confirmed by the linear dependence of σ^2 on time, shown in figure 4(b).

The important parameter D, the exciton diffusion coefficient, was obtained from these measurements by studying the slope of the σ^2–time curve in the diffusive regime [17]. This measurement gives the experimental value of D in the low exciton density limit. For DQW structures with well widths of 80, 100, 120, and 140 Å, the corresponding D were found to be (in units of cm^2 s^{-1}): 0.24, 0.74, 2.08, and 9.4. These results show that $D \propto L^6$ where L is the QW width. Similar dependence was found previously for free electrons in QW's by Sakaki *et al* in [19], which is well explained by interface roughness scattering from well width fluctuations [20–22]. This finding is a strong evidence that indeed, for dipolar excitons at low temperatures and low densities, potential fluctuations due to interface roughness is the dominant scattering mechanism.

5.2. Modelling

Using the definitions of the dipolar exciton currents in section 4, the importance of the dipole driven term, J_d, over the diffusion term, J_D, in the dynamics of free expanding excitons can be easily described by their ratio, γ,

$$\gamma(r, t) = J_d/J_D = \frac{n_X \alpha (e^{T_0/T_X} - 1)}{kT_0}. \tag{8}$$

Whenever $\gamma \gg 1$, the expansion is driven by the repulsive dipolar force. When $\gamma \ll 1$, the expansion becomes diffusive. An exciton fluid will exhibit a fast driven expansion if its initial density profile, $n_X^0 \equiv n_X(r = 0, t = 0)$, satisfies $\gamma(r = 0, t = 0) > 1$. As a dense exciton fluid starts to rapidly expand due the repulsive forces, its density will decrease and the expansion will slow down. Wherever the density decreases such that $\gamma < 1$, the expansion will become diffusive, until eventually the diffusion will dominate the dynamics of the whole exciton fluid. This picture is in qualitative agreement with the experimental observations discussed earlier.

Using the parameters extracted from the experiments, we estimate that $\gamma(r = 0, t = 0) \simeq 800$, indicating that the exciton fluid should indeed exhibit an initial fast driven expansion due to the dipole pressure, followed by a diffusive behaviour at later times. In the model calculations, we assume radial symmetry and an initial Gaussian distribution of optically excited dipolar
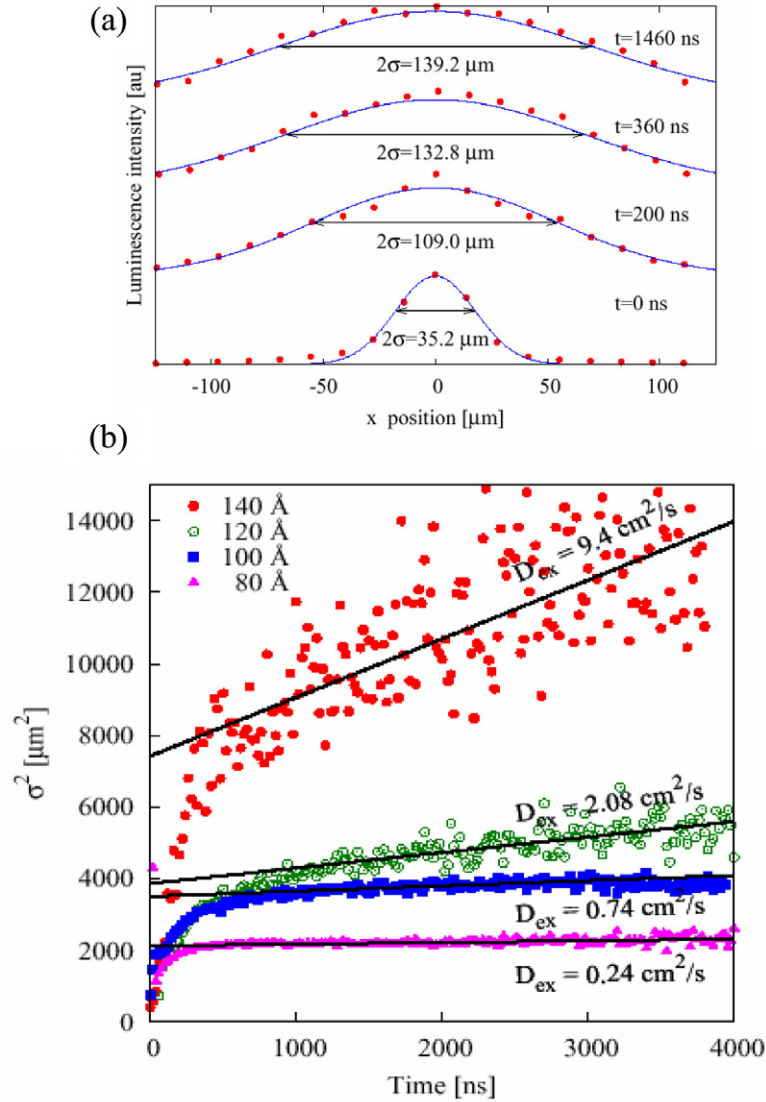
Figure 4. (a) The spatial profile of the dipolar exciton fluid at different times after the excitation. The measured luminescence intensities are normalized. The solid lines are Gaussian fits to the data. (b) The square of the width of the exciton profile as a function of time. This figure is taken from [17] with permission from the authors.

excitons, with a half-width $\sigma_0 = 15$ μm and an $n_X^0 = 10^{11}$ cm^{-2}, similar to the experimental conditions. We also use an exciton dipole length of $z_0 = 12$ nm, a lattice temperature of 3K, and an exciton lifetime of 3 μs (measured). The calculation for σ^2 as a function of time is plotted in figure 5, showing a very good agreement with the experiments by Vörös *et al* plotted in figure 4(b). The only parameters for the calculation that were not predetermined by the experiments are the exact initial density and the initial temperature of the exciton fluid. The density can be only roughly estimated from the excitation intensities quoted in [17], which indeed yields $n_X^0 \sim 1 \times 10^{11}$ cm^{-2}. Here, we assume that the optically excited electrons
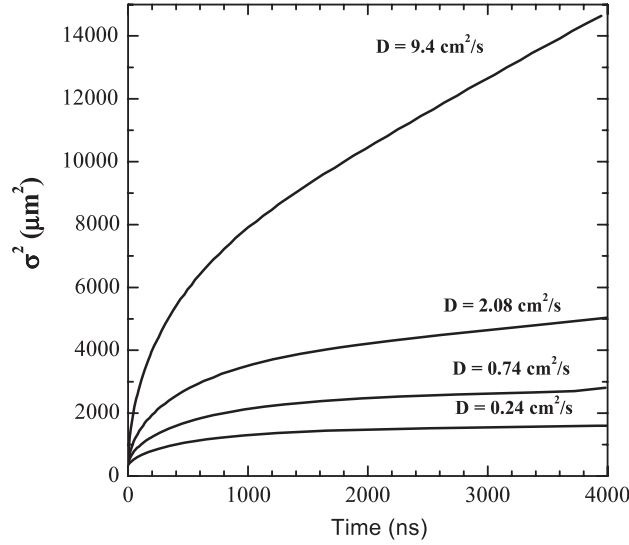
Figure 5. Calculated σ^2 of the dipolar exciton density profiles as a function of time after excitation by an optical pulse, for diffusion coefficients and experimental parameters similar to those in the experiments discussed in [17] and shown in figure 4.

and holes quickly bind into dipolar excitons with an effective temperature of 50 K determined roughly by the dipolar exciton binding energy.

A very important consequence of a fast expanding exciton fluid is the quick decrease of the dipolar exciton density, with time scales much shorter than the recombination lifetime. This fast density decrease will limit the time where the dipolar exciton density is larger than the critical quantum degeneracy density $n_X^c = g m_X k T_X / (2\pi \hbar^2)$, which marks the onset of distinguishable Bose–Einstein statistics effects, can be sustained. It turns out that the ratio between n_X^c and the critical density for the driven expansion regime, $n_d^c = k T_X / \alpha$, derived by setting $\gamma = 1$, is

$$\frac{n_X^c}{n_d^c} = \frac{2 m_X g e^2 z_0}{\hbar \epsilon} \approx 20, \tag{9}$$

for typical GaAs DQW structures. This ratio is independent of temperature, and its value suggests that a *degenerate* Bose–Einstein fluid of dipolar excitons is *always* strongly driven by the dipolar pressure.

In figure 6(a) we plot the calculated central density, $n_X(r = 0, t)$, of an expanding, initially small ($\sigma = 15 \ \mu$m) and high mobility exciton fluid ($D = 10 \ \text{cm}^2 \ \text{s}^{-1}$) as a function of time and assuming $T_X = T_l$. The calculations are performed with a lattice temperature of $T_l = 2$ K, for different initial exciton densities n_X^0. The horizontal dash–dotted line represents the critical quantum degeneracy density n_X^c. As can be seen, due to the fast initial expansion, within less than 30 ns, the density of the originally degenerate exciton fluid drops below n_X^c even for high initial densities (in this calculation, we used densities as high as $2 \times 10^{11} \ \text{cm}^{-2}$, in which the indirect excitons may not be well defined single particles anymore. In those cases, the strong Coulomb repulsion between same charge carriers will result in a qualitatively similar expansion). This time is much shorter than the exciton lifetime of 3 μs. Figure 6(b) shows similar traces for different exciton diffusion coefficients. While smaller diffusion coefficients seem to result in less expansion and thus longer times for quantum degeneracy
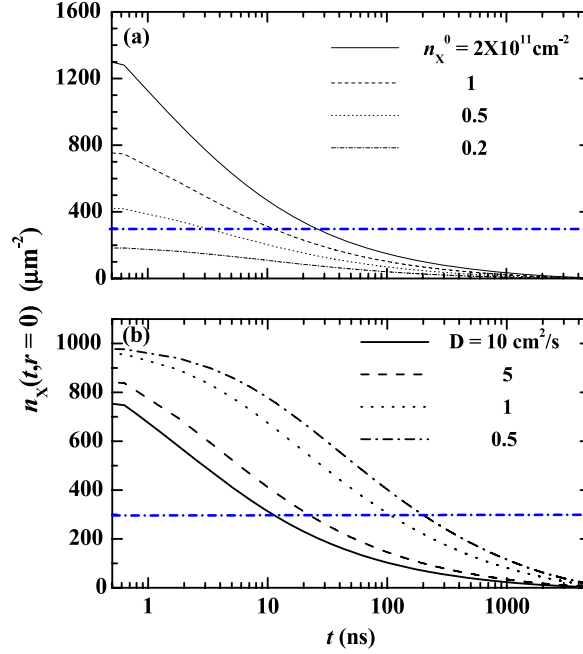
Figure 6. Calculated centre exciton densities as a function of time, $n_X(t, r = 0)$ for (a) different initial centre densities n_X^0, and (b) different exciton diffusion coefficients D. The dashed–dot lines mark the quantum degeneracy density n_X^c.

$(n_X(r = 0) > n_X^c)$, they also suggest a poor sample quality and large disorder which can strongly suppress quantum phase transitions.

The above results are summarized in figures 7(a), (b) where the time interval Δt in which $n_X(r = 0) > n_X^c$ as a function of the exciton temperature, for various D values and initial densities n_X^0 are shown. For high mobility samples, decreasing the temperature and increasing the initial density only slightly increases Δt, to values still much smaller than τ_X, as a result of the fast driven expansion. For low mobility samples, at very low temperatures, Δt can be in the microsecond range, comparable to τ_X. However, at high exciton densities, it is predicted [12] that the dipolar interaction will effectively screen the disorder, which in turn will make the fluid much more mobile, even for lower quality samples. This will increase the effective diffusion coefficient, thus again leading to fast expansion.

Figure 7(c) shows the dependence of Δt on the initial size of the exciton fluid for $D = 10$ cm^2 s^{-1} and $T_X = T_l = 2$ K. As the initial size increases (keeping the same centre density), the dipole driving force decreases $F_d \propto |\nabla n_X| \propto 1/\sigma_0$, and so does the expansion rate. Starting with large enough initial exciton fluids leads to much smaller expansion rates and thus to Δt values comparable to the exciton lifetime τ_X. This strategy is acceptable but will require large excitation powers to create a large dense exciton fluid which may lead to substantial heating of the lattice.

The above calculations show that even if the dipolar excitons immediately thermalize with the lattice, the time that the dipolar exciton fluid sustains a density above the degeneracy threshold after the excitation by an optical pulse is limited. Unfortunately, the time that the dipolar excitons can actually be degenerate is even shorter. This is a direct consequence of the fact that initially the optically excited dipolar excitons are much hotter than the actual

11
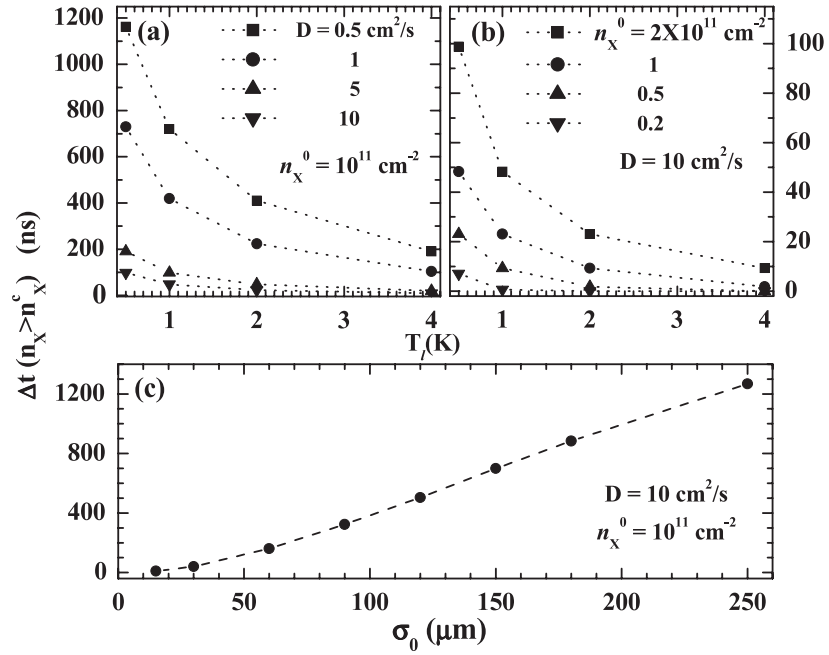
Figure 7. Time interval Δt in which the centre dipolar exciton fluid density, $n_X(r = 0)$, at $T_X = T_l$ is larger than the quantum degeneracy density, n_X^c, as a function of the lattice temperature, T_l. (a) shows the results for different diffusion coefficients, D while (b) shows different initial centre densities, n_X^0. (c) shows Δt as a function of the initial size of the exciton fluid for $T_X = T_l = 2$ K.
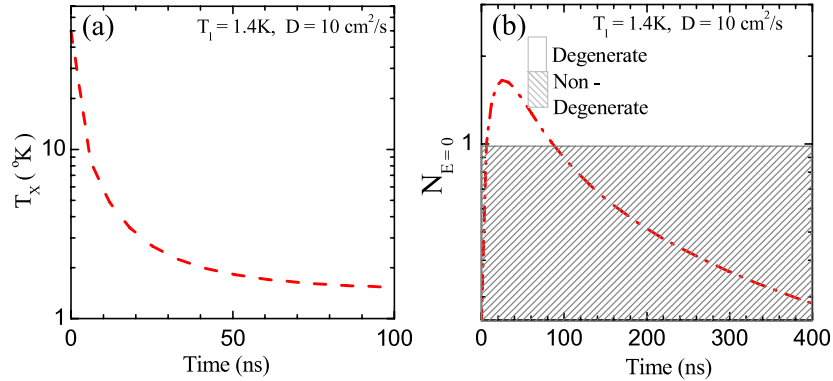
Figure 8. Calculated (a) temperature, and (b) ground state occupancy evolution of a free expanding dipolar exciton fluid.

lattice temperature and of the additional heating in the expanding exciton fluid caused by the conversion of the exciton dipole repulsion energy into thermal energy of the excitons via exciton–exciton scattering [14, 18].

The calculated temperature evolution of the exciton fluid is plotted in figure 8(a). Here we assume the dipolar excitons are created hot with a temperature of 50 K and that the exciton–lattice thermalization time is $\tau_l = 1$ ns. We used a T_l of 1.4 K and a D of 10 cm^2 s^{-1} for this calculation. The calculation shows that the expansion induced heating dramatically

slows down the exciton cooling, which would happen on a timescale determined by τ_l if the expansion induced heating was not present. Using this calculated exciton temperature and density evolution, the 2D exciton quantum degeneracy or the ground state occupation number, $N_{E=0} = (\exp(T_0/T_X) - 1)$, can be determined. Figure 8(b) shows $N_{E=0}$ as a function of time for the expanding excitons. We see that although τ_l is short, $N_{E=0}$ rises much slower initially, due to both the extra heating and the decreased density, both of which result from the exciton expansion. Figure 8(b) shows the time that the excitons are degenerate (with $N_{E=0} > 1$) is on the order of tens of nanoseconds only, and that the degree of degeneracy is not very high. Another possibility is to use CW excitation, thus preventing the fast density depletion by continuously supplying new excitons. The analysis of the advantages and limitations of such CW excitation method will be discussed in section 8.

6. Excitons in electrostatic traps

The analysis in section 5 shows that at least for the case of pulsed excitation, the free expansion driven by the strong dipole–dipole repulsion severely limits the capability of creating a dense dipolar exciton fluid for a long period of time using tightly focused beams. There are two strategies to keep a high mobility dipolar exciton fluid from too much expansion. The first is to strongly defocus the optical pulses and excite an initially very large exciton fluid, thus suppressing the density gradient and the fast expansion. This approach, however, is not favourable since it involves high overall excitation power which could lead to complications such as increased lattice temperature. The other strategy is to design an artificial spatial confinement for the dipolar excitons in the QW plane. Such spatial confinement creates exciton traps that can prevent the excitons from expanding and keep them dense with a reduced total number of excitons and therefore much lower total excitation power. This advantage of achieving high density dipolar exciton fluid with a reduced excitation power also applies to the steady state case where a CW excitation is used. A high density steady state dipolar exciton fluid can be achieved without any trapping, but the excitation power needed to compensate for the effect of the exciton fluid expansion is much higher than that needed for the same exciton density in a trap.

A small exciton trap not only helps to reduce the required optical excitation power for achieving high densities, it is also predicted to increase the temperature for a phase transition to a condensed state [12]. Furthermore, as we will show later, some trap designs result in a spatially homogeneous distribution of excitons within the trap boundary, creating a 'pool' of excitonic fluid. Such a fluid is very interesting from both thermodynamics and hydrodynamics points of view.

The trapping of dipolar excitons can be achieved by either introducing a local strain into the QW's, a technique currently used by the Pittsburgh group [23], optically induced traps [24], or using local electrostatic gates to create spatially varying electric fields [25–29], the approach that we took in our own experiments. As we will show, electrostatic traps have a flat profile and a sharp boundary. They can be effectively controlled in depth and spatial extent, and can be reconfigured quite fast.

In this section, we first discuss the basic concept of operation and issues related to a design of effective electrostatic traps. We then show the modelling of the dynamics of dipolar excitons in a trap. Finally, we present experimental results showing that these traps indeed confine a stable, high density dipolar exciton fluid for a time comparable to the intrinsic dipolar exciton radiative lifetime, τ_X. The electrostatic trapping therefore represents a promising way of studying the complex thermodynamic phases of interacting dipolar excitons.
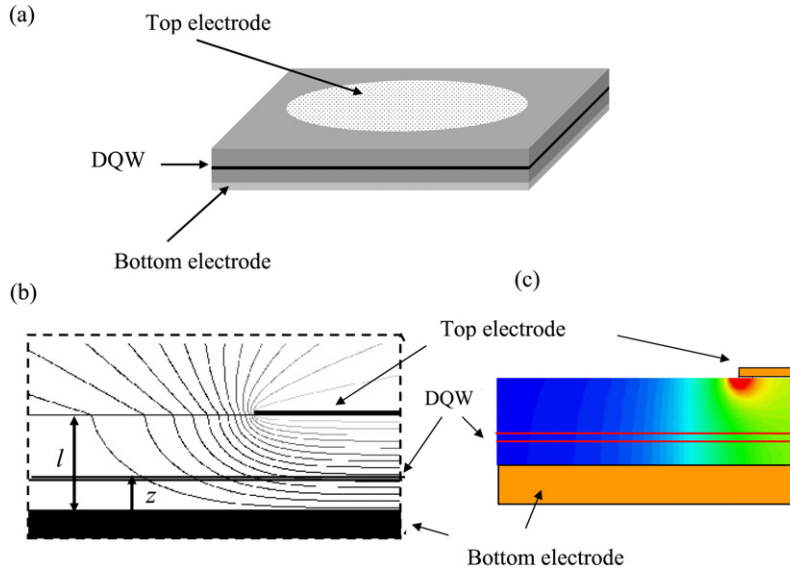
Figure 9. (a) An illustration of a suggested dipolar electrostatic trap design. (b) Calculated equipotential lines, and (c) calculated total electric field distribution close to the edge of a circular trap with $R/l = 10$.

6.1. Concept and design

The idea of electrostatic trapping is straightforward [25, 29, 30]. It utilizes the fact that the dipolar excitons that are aligned perpendicular to the plane of the QW's are high field seekers: they tend to stay at positions with lower potential where the electrical field parallel to the dipole moments is higher. A high field region (trap) is easily realized using a local electric gate. Consider a geometry where the extended metallic film contact used in the free exciton expansion studies is reduced to a small circular gate with a radius R, as illustrated in figure 9(a). Applying a sufficient voltage between the top and bottom electrodes creates higher field and therefore lower potential for the dipolar excitons under the circular gate. The trapping potential profile is determined by the field distribution via

$$\varepsilon_t = \vec{d} \cdot \vec{E}(r, z) = \mathrm{d}E_z(r, z), \tag{10}$$

where $\vec{d} = -ez_0\hat{z}$ is the exciton dipole moment, $\vec{E} = -\nabla\phi$ is the applied electric field, r is the in-plane radial coordinate with its origin at the centre of the circular top gate, and z_0 is the effective separation between the electron and the hole and is equal to the separation between the centres of the two QW's to a good approximation. At the centre of the gate, $\vec{E}(r = 0) \equiv \vec{E}_0 = -\phi_0/l\hat{z}$, where ϕ_0 is the potential difference applied between the top gate and the bottom electrode.

Figures 9(b) and (c) show the electrostatics with the equipotential lines and total electric field distribution illustrated, respectively. Here, as an example, we used a geometry where $R = 5\ \mu\mathrm{m}$, $l = 0.5\ \mu\mathrm{m}$ ($R/l = 10$), $z_0 = 100$ Å and $\triangle\phi_0 = 1$ V. The confining potential energy for dipolar excitons, ε_t, is depicted by the solid line in figure 10 as a function of r. The maximal trapping energy at the centre of the trap is $\varepsilon_t^0 = -ez_0\triangle\phi_0/l$. The dipolar excitons experience a trapping force mostly near the sharp boundaries given by

$$F_t(r, z) = d\frac{\partial E_z}{\partial r}\hat{r} \tag{11}$$

as illustrated by the dotted line in figure 10.

14
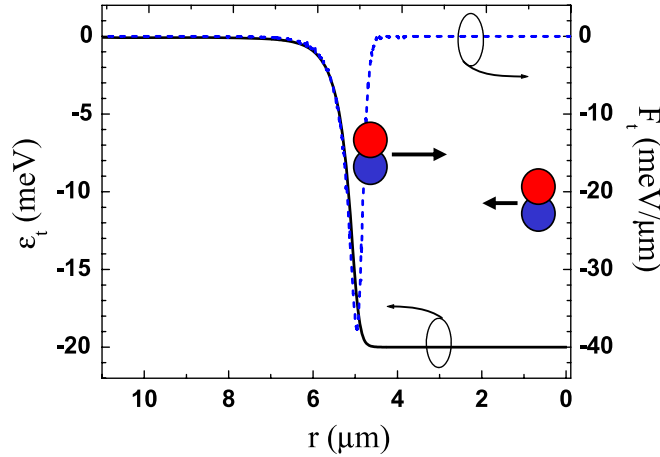
Figure 10. Calculated confining energy for dipolar excitons (ε_t, solid line) and force (F_t, dashed line) for a circular trap with $R = 5 \ \mu$m, $l = 0.5 \ \mu$m, a potential difference $\triangle\phi_0$ of 1 V and a dipole length $z_0 = 100$ Å. The pairs of circles schematically represent dipolar excitons which experience a trapping force at the trap boundary and an outward expansion force inside the trap due to the dipolar repulsion.

Ideally, for $R \gg l$, such a trap behaves like a 'pool' of free moving excitons, subject to perfectly reflecting boundary conditions at the edges (one can get a non-flat potential well for $R \sim l$). As the exciton density within the trap increases, the interaction between the dipolar excitons, $\varepsilon_d(n_X)$, given by equation (1), effectively screens the electric field from the electrodes, leading to higher potential for the dipolar exciton fluid. In the case that $\varepsilon_t > \varepsilon_d$, the excitons will be confined within the boundaries of the trap being reflected from the walls by the trap's dipole force. As the exciton density becomes large enough to yield $\varepsilon_t \cong \varepsilon_d$, the external field applied via the electrodes will be completely screened and the dipolar excitons will experience no trapping force and will spill over, with much shorter lifetimes as they become more direct. This condition for trapping can be expressed as

$$|\varepsilon_t/\varepsilon_d| > \vartheta \tag{12}$$

where ϑ is a parameter larger than but of order 1, which determines by how much 'residual' trapping energy is required in the experiment in order to keep the dipolar exciton radiative lifetime, τ_X, long enough. It is straightforward to see that the maximal trapped exciton density for a given applied potential difference ϕ_0 is:

$$n_X^{max} = \frac{\epsilon\phi_0}{4\pi \, el\vartheta}. \tag{13}$$

Here, we have neglected the possible 'spill' of dipolar excitons due to the thermal energy kT_X since it is always much smaller than ε_{dd} at temperatures and densities relevant for exciton quantum degeneracy.

To confine excitons with a desired density, the above discussion suggests that one only needs to apply an external potential difference large enough to make the potential trap deeper than the dipolar interaction energy. Unfortunately, we have so far ignored the electric field component *in the QW plane* near the trap boundary, E_r, which increases with an increasing applied potential difference. This radial field will tend to pull the electron and the hole into opposite directions and thus ionize the excitons [31, 25], reducing the total exciton density and giving rise to an effective lifetime of excitons in the trap, τ_{trap}, which we have derived

analytically in [30]. Thus, to achieve a dense and long lived dipolar exciton fluid, it is essential that E_r and therefore the external potential difference do not exceed the level which makes the effective trap lifetime shorter than the time required for exciton cooling and thermalization.

The constraint on the trap performance now becomes obvious: for a desired exciton density in the trap, there is a minimum required vertical field in order to get the trapping energy ε_t larger than ε_d. This requirement will introduce a radial field which in turn will increase the ionization rate at the trap boundaries and will reduce the effective trap lifetime. This constraint is shown by the calculated curves in figure 11(a) for different sample structures characterized by different z/l value. The x-axis gives the dipolar exciton densities one wishes to achieve (or equivalent, the trap depth ε_t) and the y-axis shows the resulting effective trap lifetime. It can be readily seen that as the desired exciton density increases, the effective trap lifetime deteriorates. This will dramatically reduce the time available for exciton thermalization even if their intrinsic lifetime is very long, and will dramatically increase the optical power required to achieve such densities. Most importantly, the effective trap lifetime improves exponentially for structures with smaller z/l value, in which the DQW is closer to the bottom substrate and the in-plane ionizing field is smaller.

Reversing the above analysis, the requirement that the effective trap lifetime τ_{trap} be longer than 1 μs (comparable to the dipolar exciton recombination lifetime and desirable for exciton thermalization and cooling) puts an upper limit on the applied potential difference, and consequently limits the maximum achievable exciton density. This maximum density, n_X^{max}, as a function of z/l is shown by the solid line in figure 11(b). For densities beyond this maximum, the applied bias becomes too large and the trap becomes ineffective due to the exciton ionization. The upper bound of achievable densities implies an corresponding maximal lattice temperature required to achieve degeneracy. This temperature requirement as a function of z/l is shown by the dashed curve in figure 11(b).

Figure 11(b) shows that as the DQW's gets further away from the bottom electrode, there is a strong reduction of n_X^{max} due to the increased in-plane electric field. The guideline for designing a trap for a high density dipolar exciton fluid is then to minimize z/l as much as possible. In practice however, a sample with the DQW's too close to the n-doped substrate may suffer from other problems such as unwanted doping of electrons. Thus while we need to keep z/l small, z has a practical minimum value which will then determine the total sample thickness, l. Our calculation shows that z/l should be smaller than 0.25 for an exciton density larger than 10^{10} cm^{-2}, for which the lattice temperature required for degeneracy is still achievable in the laboratory. We have designed and grown a set of samples with various z/l values, the smallest of which has $z/l \approx 0.01$. For the small z/l samples the in-plane field is small enough that an exciton fluid with densities up to $\sim 10^{11}$ cm^{-2} can be confined without significant ionization, thus covering the whole density range up to the Mott transition density, where excitons transform to e–h plasma. In section 6.3, we will discuss measurements from such samples. Details on how to calculate the in-plane field, the exciton ionization rate, and the effective trap lifetime can be found in [30].

6.2. Modelling

The general model of section 4 can now be used to calculate the effect of the trapping potential. This section discusses calculations showing that the electrostatic trap can indeed confine a spatially uniform dipolar exciton fluid with densities way above the threshold value for quantum degeneracy for a period of the order of the exciton recombination lifetime, τ_X.

Compared to the free expanding case, the effect of the electrostatic trapping is included in the third term for the exciton current, J_{ext}, in equation (6) for the dipolar exciton density
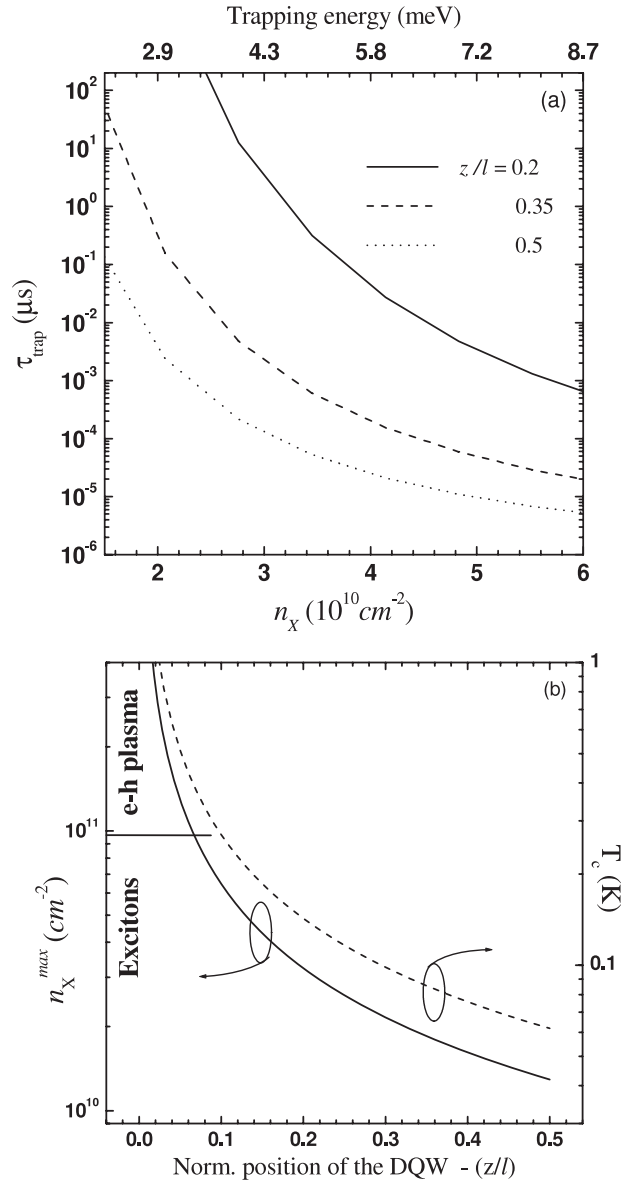
Figure 11. (a) Effective trap lifetime as a function of the desired trapped density n_X and the trap energy $\varepsilon_t(r = 0)$ for various vertical positions of the double QW structure in the trap, z/l. Here $R/l = 50$, and $\vartheta = 1.2$. (b) The calculated maximal density (solid line) of trapped dipolar excitons (with same parameters as in (a)), and the expected Bose–Einstein condensation transition temperature (dashed–dot line), as a function of z/l. The horizontal line marks the approximated Mott density.

dynamics. This exciton current is driven by the trapping force of equation (11), as a result of the electrostatic trapping potential shown, for example, by the solid line in figure 10. For calculation convenience, we approximate this potential profile with an analytic function: $\varepsilon_t(r) = \frac{\varepsilon_t^0}{2}(1 + \tanh\frac{2(r-R)}{\delta})$. Here, ε_t^0 is the potential energy at the trap centre (see section 6.1) and δ is the effective 'thickness' of the boundary region, determined by the distance between the
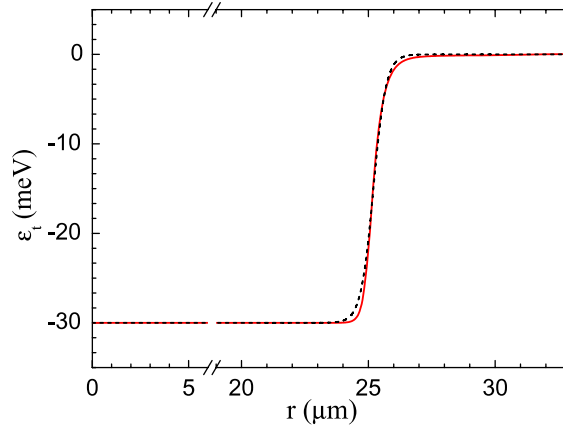
Figure 12. The calculated potential radial profile (solid line) and its analytic approximation (dashed line) for an electrostatic trap.

top gate and bottom electrode. This approximation is fairly accurate as illustrated in figure 12 where the numerically calculated and the analytically approximated potential profiles are shown by the solid and dashed lines, respectively. The resulting exciton current due to trapping is: $\mathbf{J}_{\text{ext}} = -\mu n_{\text{X}} \frac{\varepsilon_t^0}{\delta}[1 - \tanh^2 \frac{2(r-R)}{\delta}]\hat{\mathbf{r}}$. The other two terms in equation (6) for excitons in an electrostatic trap are similar to those for the case of free expanding dipolar excitons. The dipolar exciton lifetime here becomes position dependent, having different values inside the trap, on the trap boundary, and outside of the trap.

In the following calculations, the size of the trap is taken as $R = 25\ \mu$m, and the depth of the trap is fixed at $\varepsilon_t^0 = 30$ meV (consistent with our experiments). Similar to the free exciton expansion calculation, we assume that a pulsed (~ 1 ns) optical excitation creates dipolar excitons at the centre of the trap with a Gaussian profile: $n_{\text{X}}(r, t = 0) = n_0 e^{-r^2/w_0^2}$, where, as is typical for our experiments, $w_0 = 15\ \mu$m and $n_0 = 1.5 \times 10^{11}$ cm^{-2}. The position dependent exciton lifetime, τ_{X}, is taken to be 1.5 μs inside the trap, similar to experimentally measured values for dipolar excitons under similar bias voltage. Outside the trap, the excitons are direct and their lifetime is taken as $\tau_{\text{X}} = \tau_{\text{X}_{\text{D}}} = 0.1$ ns. In the trap boundary region, the effective τ_{X} is calculated using the exciton ionization rate determined by the in-plane electric field, as detailed in [30].

Figure 13(a) plots the radial density profile of the dipolar excitons in a high quality electrostatic trap with negligible boundary ionization, in which case the exciton lifetime in the trap boundary region is only limited by the intrinsic lifetime of the excitons. The values of the diffusion coefficients are determined by the free exciton expansion experiments discussed in section 5. Figure 13(a) shows that within tens of nanoseconds the profile flattens, as the driven expansion by the dipole repulsion pushes the excitons to the reflecting trap boundary. The competition between the repulsion and trapping force results in a stable flat exciton density profile (the density profile with the lowest total energy) that decays with the characteristic radiative lifetime of the excitons, τ_{X}.

The result above shows that an electrostatic trap with negligible boundary ionization is effective in confining a spatially uniform dipolar exciton fluid with densities of $\sim 10^{11}$ cm^2 for a time comparable to τ_{X}. This is strikingly different from either a free expanding dipolar exciton fluid discussed previously or dipolar excitons in a low quality trap with a considerable boundary ionization, as depicted in figure 13(b), in which a comparison of the exciton profiles
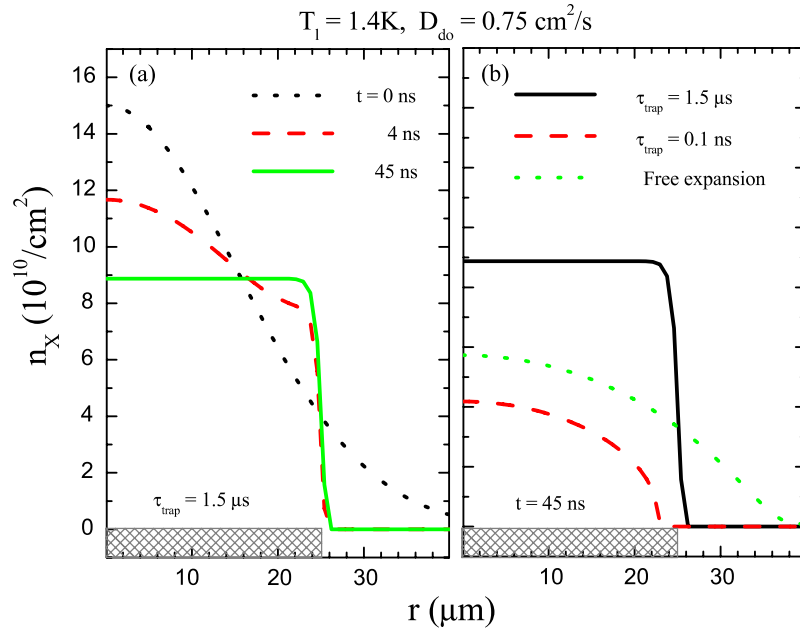
Figure 13. Radial profile of the dipolar exciton density distribution for (a) a high quality electrostatic trap ($\tau = 1.5\,\mu$s in the trap boundary region) at various times, and (b) high quality trap (solid line), low quality trap ($\tau_X = 0.1$ ns in the boundary region, dashed line), and free expanding excitons (dotted line) at $t = 45$ ns. The bar at the bottom of each figure mark the radial extent of the trap.

at 45 ns after the excitation is shown for the three cases. In the case of free expanding excitons, the density rapidly decreases, as the driven expansion continues to spread the exciton fluid to large radii. For a low quality trap ($\tau_{\text{trap}} = 0.1$ ns), excitons reaching the trap boundaries are effectively eliminated by ionization, depleting the overall exciton density much quicker. Note that in this case, the exciton profile remains curved and does not flattens like the exciton pool in the high quality trap. The lack of this curvature can be used as a supporting experimental evidence that a trap indeed has low boundary ionization, as will be shown later.

The cooling and thermalization of this confined fluid of dipolar excitons are governed by the temperature equation, equation (7). The equation is similar to that used for the free expanding excitons. Again, the initial exciton temperature is taken to be T_X ($t = 0$) $\simeq 50$ K, much hotter than the lattice temperature $T_l = 1.4$ K. The 2D exciton degeneracy or the ground state occupation number, $N_{E=0}$, is easily determined using the calculated exciton density and temperature.

To see the dramatic effect of the trapping on the quantum degeneracy of dipolar excitons with high mobility ($D_{\text{do}} = 10$ cm^2 s^{-1}), we show in figure 14(a) the calculated $N_{E=0}$, as a function of time after photoexcitation, for excitons in a high and low quality electrostatic trap compared to that of free expanding excitons calculated previously. Initially, the ground state occupation is much smaller than unity, as the excitons are hot and essentially classical. The exciton fluid then starts to expand and cool. As the transition to a distinctive Bose–Einstein statistics arises when $T_0/T_X \sim 1$, there is a competition between cooling that tends to increase $N_{E=0}$ and expansion that tends to decrease it due to the drop of n_X. In a high quality electrostatic trap, the expansion of the dipolar excitons is limited to the trap boundaries, and thus reaches steady state after $\sim$10 ns. After that, the heating due to dipole potential which

19
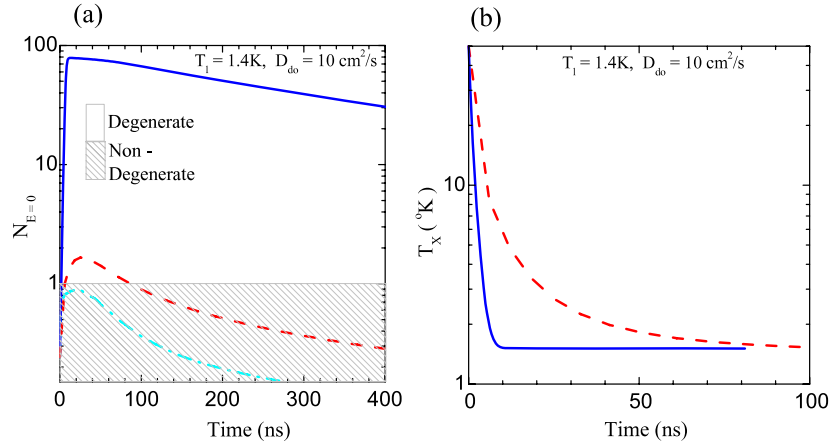
Figure 14. (a) The exciton ground state occupancy, $N_{E=0}$, as a function of time for a high quality trap ($\tau_{\text{trap}} = 1.5$ μs, solid line), a low quality trap ($\tau_{\text{trap}} = 1$ ns, dash–dotted line) and free expanding excitons (dashed line). The cross-hatched area marks the non-degenerate region. (b) The temperature evolution for dipolar excitons in the high quality trap (solid line) and free expanding excitons (dashed line).

is significant for a free expanding excitons is absent. Cooling is therefore efficient, as is seen in figure 14(b), and the excitons reach a stable highly degenerate state with $N_{E=0} \gg 1$, that decays slowly on the timescale of τ_{X}. On the contrary, if the excitons are freely expanding (no trap), their density continues to drop as they expand. While they continue to cool by interaction with the lattice, the expansion itself heats up the fluid, as more internal potential energy is lost and converted into heat by the fast exciton–exciton scattering. This leads to a slower net cooling rate for the free expanding excitons compared with the trapped ones, and consequently the excitons reach only marginal quantum degeneracy before their density drops too low due to the fast driven expansion. Finally, in a low quality trap, the drop in exciton density due to boundary ionization dominates over the cooling, completely preventing the excitons from reaching quantum degeneracy.

These calculations strongly suggest that the creation of a stable and long lifetime highly degenerate dipolar exciton pool is of close reach with the help of the electrostatic trapping. The above analysis is based on an critical assumption that the cooling rate is much shorter than the exciton lifetime. While this is very reasonable (see [15]), it is now up to the experiments to verify this assumption by revealing evidence of Bose–Einstein statistical effects.

6.3. Experimental results

In this section, we discuss experiments performed on dipolar excitons in electrostatic traps following the design discussed in section 6.1. These results show compelling evidence for the successful implementation of the electrostatic trapping scheme, in which a high density, stable, and spatially uniform exciton fluid is maintained in a truly confined and controlled configuration [32]. In fact, for at least half a microsecond, the dipolar exciton fluid sustains a density higher than the critical density for degeneracy if the exciton fluid temperature reaches the lattice temperature within that time. It is therefore possible that the excitons are indeed degenerate although we have not yet observed a definite and unambiguous signature of Bose–Einstein statistics.

The GaAs/AlGaAs DQW structures used for the measurements is similar in design to those discussed in section 5 and figure 2. We will discuss measurements performed on two samples:
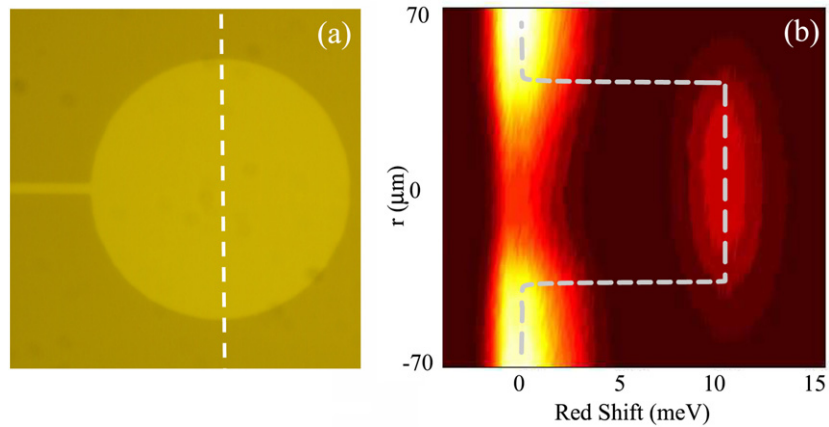
Figure 15. (a) An optical image of the top gate of an electrostatic trap. (b) Spatially resolved emission spectra from an 80 μm trap (sample A) collected from a radial cross-section of the top gate along the dashed line showing in (a). The dashed white line in (b) is the calculated potential profile for the dipolar excitons. The energy axis shows the red-shift of the emission from the direct exciton emission line whose actual position is at 1.5567 eV (797 nm).

one (sample A) has $z/l \simeq 0.03$ while the other (sample B) has $z/l \simeq 0.3$. The purpose is to show the difference between samples with high and low exciton ionization near the trap boundary.

We first measure the trap energy profile by spatially resolving the emission spectrum of the dipolar excitons. The emission is collected along the radial cross-section of the trap gate shown in figure 15(a) and is dispersed by a spectrometer. An example of such spectral image is shown in figure 15(b), taken from an 80 μm diameter trap of sample A at $T = 5$ K with an applied bias of 3 V, excited using a defocused CW He–Ne laser. The confining potential profile can be clearly seen from the red-shifted emission under the gate. The emission energy outside the trap corresponds to zero field, or direct exciton line at 1.5567 eV. The white dashed line is the calculated trap potential, which nicely fits the experimental data. The emission from inside the trap appears dimmer due to the semitransparent metallic trap gate which blocks most of the optical excitation into the trap as well as most of the trap emission.

The effect of a non-negligible in-plane electric field near the trap boundary is to ionize the dipolar excitons into opposite charges which are pulled to different directions. This will unavoidably result in an accumulation of unbalanced charges outside the trap which will in turn affect the exciton formation and their emission characteristics outside the trap. Based on this analysis, we developed a spatially resolved 'excitation pump–probe' technique to estimate the extent of the exciton ionization. In particular, an 'excitation pump' from a non-resonant CW He–Ne laser, is focused to the centre of a trap ($r = 0$). An additional, similar but weak 'excitation probe' beam is focused outside the trap where no external bias was applied. The experimental geometry is shown in figure 16(a). The idea is that the excitons created inside the trap may undergo ionization at the trap boundary, and the ionized charged carriers that will drift outwards and accumulate outside of the trap will affect the emission spectrum of excitons created by the spatially remote excitation probe. Figures 16(b), (c) and (d), (e) present the spectral image taken from a 50 μm diameter electrostatic trap from sample A ($z/l = 0.03$) and B ($z/l = 0.3$), respectively. The images were taken with the excitation pump either on or off. For the *entire* range of pump excitation powers and gate bias, we find that the probe PL is independent of the presence of the excitation pump for sample A, even for excitation probe
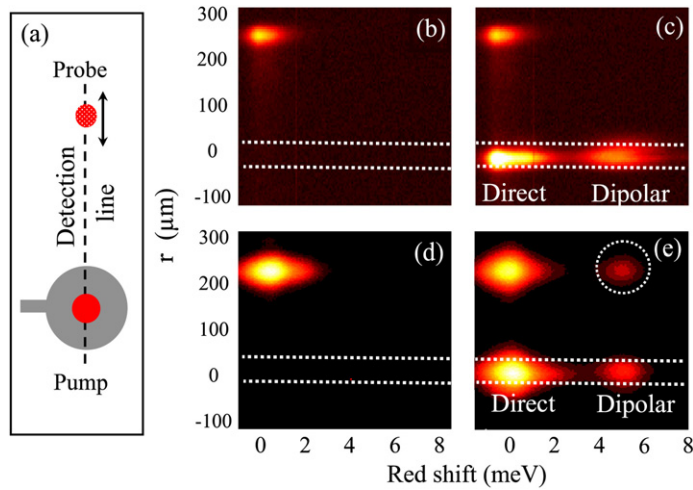
Figure 16. (a) Geometry of the PL pump–probe experiment on a 50 μm diameter trap. The PL is spatially resolved along the dashed line with its energy shown as a red-shift from the direct exciton line. (b) and (c) show the emission spectral images from sample A with the excitation pump off and on, respectively. The pump power is 30 μW and dipolar exciton red-shift is 5 meV. (d) and (e) show emission spectra for sample B with the excitation pump off and on taken under identical conditions. The white dotted lines mark the trap boundary. The low energy probe PL line (inside the white circle in (e)) indicates that sample B is 'leaky', as expected from its design (see text).

positions very close to the trap boundary. It always corresponds to the transition energy and lineshape of direct excitons, consistent with the zero bias conditions expected outside of the trap and is an indication of the high quality of the trap boundaries in sample A. On the contrary, the probe PL behaviour of sample B ($z/l = 0.3$) is remarkably different: with excitation pump off, the emission of the probe excitons is similar to that observed in sample A. However, as the excitation pump beam is turned on, we observe an additional probe emission peak at the lower energy side of the direct exciton emission line, as marked by the dashed circle in figure 16(e). This dramatic change of the remote probe emission can only be explained by a *leakage of carriers* from the trap to the location of the probe, changing the local electrostatic environment and thus affecting the emission.

The distance to which the ionized carriers can extend outside a low quality trap can be investigated by moving the excitation probe to different distances away from the trap and monitor the excitation probe induced emission while keeping the excitation pump on in the trap. We observed that the extra line discussed above in sample B (with the peak marked by the dashed circle in figure 16(e)) gradually shifts to blue (towards the direct exciton line) as the excitation probe moves away from the trap boundary. This is shown in figure 17, in which the spectral positions of the extra peak, measured by its relative red-shift from the direct exciton line, are plotted as a function of the distance of the excitation probe from the trap centre. The excitation pump is maintained at 30 μW in the centre of the trap. We see that in this steady state case, the carriers leaking from a low quality trap can extend extremely far away from the trap boundary, affecting the excitation probe induced emission. All of the measurements above confirm our design rule in which z/l of the structure needs to be minimized.

A comparison between the spectral images taken from a free expanding exciton fluid and excitons in a 50 μm electrostatic trap of sample A (a high quality trap) is shown in figures 18(a) and (b). The dashed lines mark the boundary of the trap. Again, the vertical axis shows the
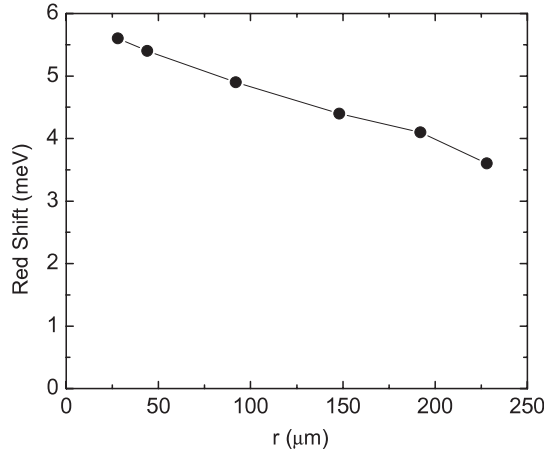
Figure 17. The spectral position of the peak marked by the dashed circle in figure 16(e) as a function of the distance of the excitation probe from the trap centre of sample B. An excitation pump of 30 μW is kept on at the centre of the trap. The energies are measured as red-shifts from the direct exciton line.
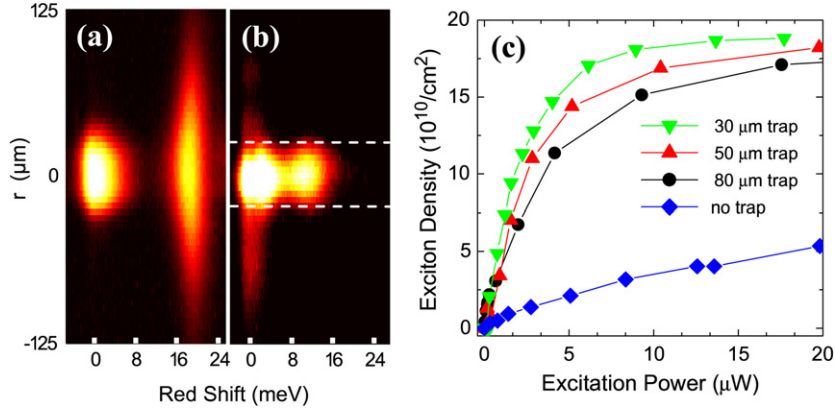

Figure 18. (a) Spatially resolved emission spectra of (a) free expanding dipolar excitons, (b) dipolar excitons confined in a 50 μm trap, with a CW He–Ne laser excitation. The emission lines at a zero red-shift are due to the direct exciton emission. The bias is 4 V and the excitation power is 30 μW. The dashed lines mark the trap boundaries. (c) The extracted dipolar exciton density at the centre of the excitation spot as a function of the CW laser excitation power on the sample surface for free expanding and trapped excitons. The applied bias is 6 V.

spatial extent of the dipolar excitons and the horizontal axis represents the emission energy, measured as red-shift relative to the direct exciton transition energy. The red-shift is due to a combination of the externally applied electric field and the screening of the external electric field by the excitons. While an increase of the external field will increase the red-shift, an increase in the dipolar exciton density will decrease it. The amount of the red-shift can be used as a measure of the dipolar exciton density, as we can write:

$$\Delta\varepsilon = -\varepsilon_{\text{ext}} + \varepsilon_{\text{d}}(n_{\text{X}}). \tag{14}$$

Here $\varepsilon_{\text{ext}} = |ez_0\Delta\phi_0/l|$ is due to the externally applied field and $\varepsilon_{\text{d}}(n_{\text{X}})$ is given by equation (1). Hence, for a given external bias and thus a given ε_{ext}, the higher the dipolar
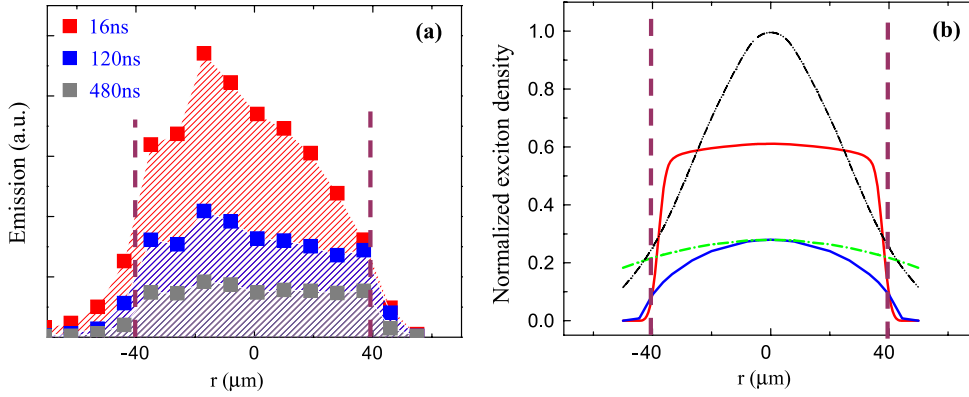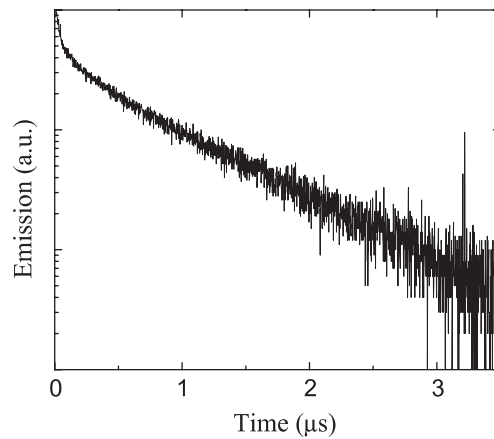
Figure 19. (a) Spectrally integrated intensity of the dipolar exciton emission along a radial cross-section of an 80 μm trap of sample A with a potential depth of 30 meV, for three different times after the initial excitation. (b) Calculated exciton density 120 ns after excitation for the case of reflecting trap boundaries (solid red), absorbing trap boundaries (solid blue), and no boundaries (dash–dot green). The black dash–dotted curve presents the initial exciton distribution.

exciton density, the larger the ε_d and the smaller the red-shift. We thus measure the red-shift at every excitation power and then we use equation (14) together with equation (1) to extract an estimate of the exciton density.

We can see from figures 18(a) and (b), that compared to the free expanding dipolar excitons, dipolar excitons in the trap under similar conditions do not expand beyond the boundary of the trap and their density is much higher (a smaller red-shift indicates a larger ε_d and thus higher n_X). This is shown more clearly in figure 18(c) which plots the estimated dipolar exciton density as a function of the excitation power for excitons in traps of various sizes and for free expanding excitons.

Note that equation (1) and thus the linear dependence of the repulsion energy on the dipolar exciton density is correct only if we neglect correlations between the particles in the fluid. While this assumption should hold well at low exciton densities, it may not hold at high densities and low temperatures due to possible carrier correlations. The saturation of the red-shift decrease (or the exciton density increase) at high excitation powers in figure 18(c) may be related to such an effect.

The dynamics of the dipolar excitons in the trap can be monitored by time resolving the spatial cross-sectional profile. The calculation discussed in section 6.2 show that the exciton density profile in a trap with negligible exciton ionization near the boundary should expand within the trap quickly (due to the dipole repulsion) following an excitation by a short optical pulse. The exciton distribution should then flatten across the entire trap and decays on the timescale determined by the dipolar exciton lifetime, τ_X. Figure 19 shows the experimental verification. The emission was taken from an 80 μm diameter electrostatic trap (biased at 6 V giving a trap depth of $\sim$30 meV) of sample A, after a short pulse excitation (pulse width 2 ps, FWHM $\simeq$ 40 μm), resonant with the direct exciton transition. The emission was spectrally integrated over the whole dipolar exciton spectral line. In figure 19(a) the exciton profile is measured at various times after the excitation, showing the expected flattening $\sim$100 ns following the initial Gaussian shape. The boundary of the trap is marked by the dashed lines and the exciton emission intensity drop at the trap boundary is sharp, limited only by the imaging resolution. The dipolar exciton density immediately after the laser excitation pulse is estimated to be $\sim$8 $\times$ 10^{10} cm^2. The time trace of the emission at the centre of the trap plotted

Figure 20. The time trace of the spectrally integrated PL at the centre of the trap studied in figure 19.

in the figure 20 implies that the exciton density decays exponentially with a microsecond time constant after the profile has flattened. This decay time, τ_{trap}, is similar to the intrinsic lifetime of the dipolar excitons, τ_X, measured for free expanding dipolar excitons in the same structure. It strongly suggests that exciton loss due to ionization at the electrostatic trap boundary in sample A is negligible. The above results depict a picture of a uniform and stable exciton fluid maintained at high density for a long period of time, determined by the exciton radiative lifetime.

Finally, we would like to show the potential of high speed manipulation of the dipolar exciton fluid inside an electrostatic trap of an InGaAs DQW structure. As an example, we show that the depth of these electrostatic traps can be dynamically reconfigured on a short timescale. We sharply modulate the bias voltage between two values at various frequencies (with a rise and fall time of the driving waveform on the order of 1 ns). The dipolar exciton emission line alternates between two spectral positions. If the trap can be reconfigured as fast as the driving bias, we should then see two distinct dipolar exciton lines in a time integrated measurements. If, however, the trap cannot be reconfigured as fast as the driving bias, then dipolar excitons spend a significant portion of their time in transition from one spectral position to the other. Therefore, a plateau in between the two dipolar exciton emission peaks is expected at high modulation frequencies. We experimentally observed two distinct dipolar exciton peaks below a modulation frequency of 100 kHz and a plateau that starts to appear above that frequency. The example in figure 21(a) is a time integrated and spatially resolved spectra image for a bias modulated between 0.5 and 1 V at a modulation frequency of 100 kHz, showing the two dipolar exciton lines and the onset of the plateau in between. Figure 21(b) shows a spectrum along the centre of the trap (the solid line in figure 21(a)). A calculation of the RC time constant of the sample shows that, in the current experiment, the maximal modulation frequency is limited by the residual contact capacitance, and hence we believe that higher modulation frequencies can be achieved with small modifications of the contact geometry.

7. Excitons in rings

In the previous sections, we presented an electrostatic trapping method for achieving high density and cold dipolar exciton fluids. Another system with a potential for creating dense and cold excitons was discovered, quite incidentally, in 2002, prior to our work on electrostatic
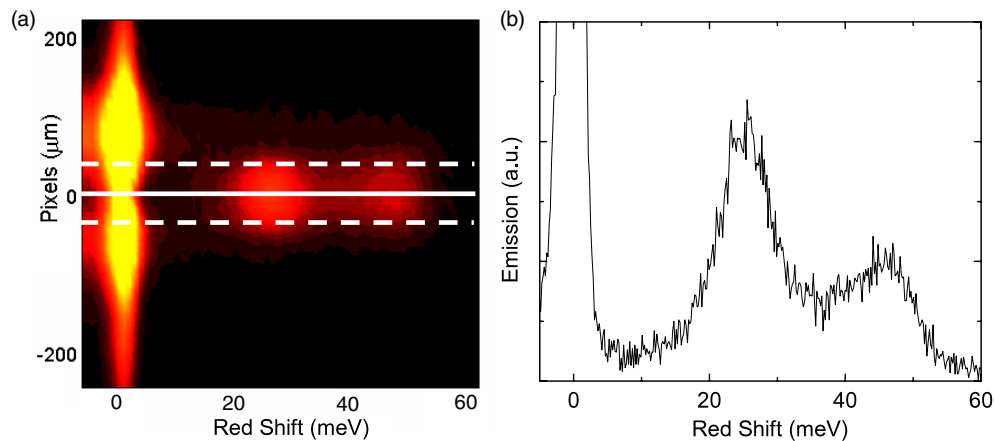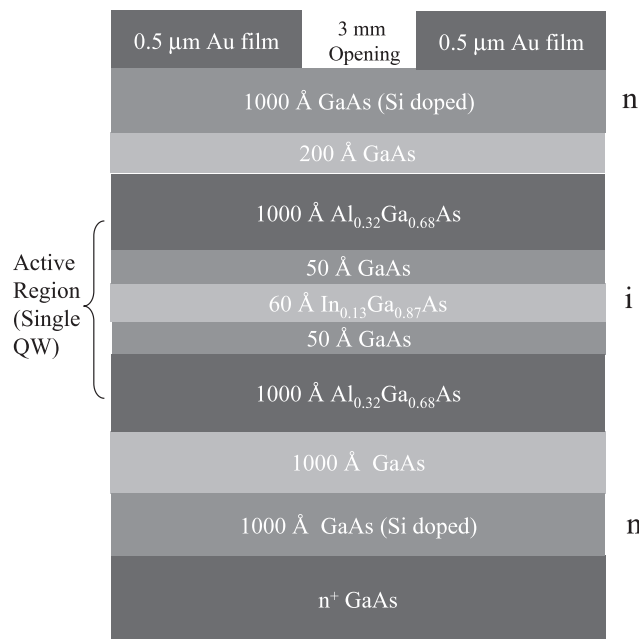
Figure 21. (a) Time integrated and spatially resolved spectrum of dipolar excitons in an electrostatic trap with a bias modulated between 0.5 and 1 V at 100 kHz (corresponding to a period of 10 μs). The dashed lines mark the trap boundary. (b) Spectrum along the centre of the trap (solid line in (a)).
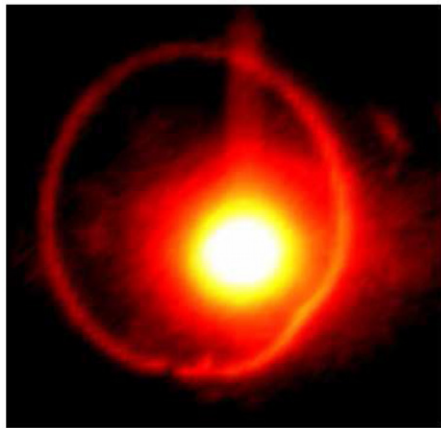
Figure 22. Photoluminescence images for single QW sample taken at an excitation power of 296 μW. The image is 700 × 700 μm. The sample was measured at $T = 8$ K, and excited with a He–Ne laser (632 nm) with a spot diameter of ∼60 μm. The sample structure is detailed in [35] and in figure 23.

trapping, and will be described in this section. Butov *et al* [33] and Snoke *et al* [34] independently observed a striking spatial emission pattern from DQW structures quite similar to those discussed above, except that the QW's were modulation doped with excess electrons via an n–i–n structure around the DQW's. In those experiments, the dipolar excitons were excited by a high energy, non-resonant and tightly focused laser beam. The observed dipolar exciton emission pattern consists of the expected emission at the excitation spot and a surprising surrounding emission ring at large radial distances, as shown in figure 22. The centre emission spot and the ring are separated by a nominally dark region. This effect was initially speculated to be a result of various exciton transport mechanisms and possibly some kind of collective coherent state of cold excitons. About a year after its discovery, a more consistent explanation

0.5 μm Au film	3 mm Opening	0.5 μm Au film	
1000 Å GaAs (Si doped)			n
200 Å GaAs			
1000 Å Al$_{0.32}$Ga$_{0.68}$As			
50 Å GaAs			
60 Å In$_{0.13}$Ga$_{0.87}$As			i
50 Å GaAs			
1000 Å Al$_{0.32}$Ga$_{0.68}$As			
1000 Å GaAs			
1000 Å GaAs (Si doped)			n
n$^+$ GaAs			

Active Region (Single QW) { (brackets the Al$_{0.32}$Ga$_{0.68}$As / GaAs / In$_{0.13}$Ga$_{0.87}$As / GaAs / Al$_{0.32}$Ga$_{0.68}$As layers)

Figure 23. The single QW structure used for studying the exciton rings.

for its origin, backed by further detailed experiments and numerical analysis, was suggested independently by us [35] and by Butov *et al* [36]. This explanation was based on an optically induced in-plane charge separation rather than the more exotic initial ideas.

While this explanation suggests that the formation of the ring itself is not a consequence of any spontaneous coherence of excitons, it does imply that the dipolar excitons formed at the ring are possibly colder than those formed at the excitation spot, making this specific system again interesting for the original purpose of obtaining dense and cold dipolar excitons. The observation of the periodical modulation of the dipolar exciton emission ring by Butov *et al* [33] in their initial experiments and the new measurements studying the spatial coherence of the emission [37] show that this approach of cooling excitons may be potentially promising. On the other hand, the charge separation can lead to large in-plane electric fields at the ring boundaries which may cause exciton ionization and reduce the effective exciton lifetime. The analysis of rings as a source of dipolar excitons will be discussed later in this section, while the trade-offs of using exciton rings as a method for obtaining cold excitons will be discussed further in section 8.

7.1. The ring formation mechanism and dynamics modelling

We start by presenting the physical origin of the ring formation. Before discussing the mechanism in detail, we note that, in our own experiments, we found that this phenomenon is not unique to double QW structures. We observed similar ring pattern in single QW structures. In fact, data in figure 22 and the rest of this section were taken from a single QW structure, as depicted in figure 23. This suggests that the ring formation does not require a long exciton lifetime.

The suggested physical mechanism is shown in figures 24(a) and (b) in the context of a single QW structure in figure 23 [35, 36], but is essentially identical in the case of DQW
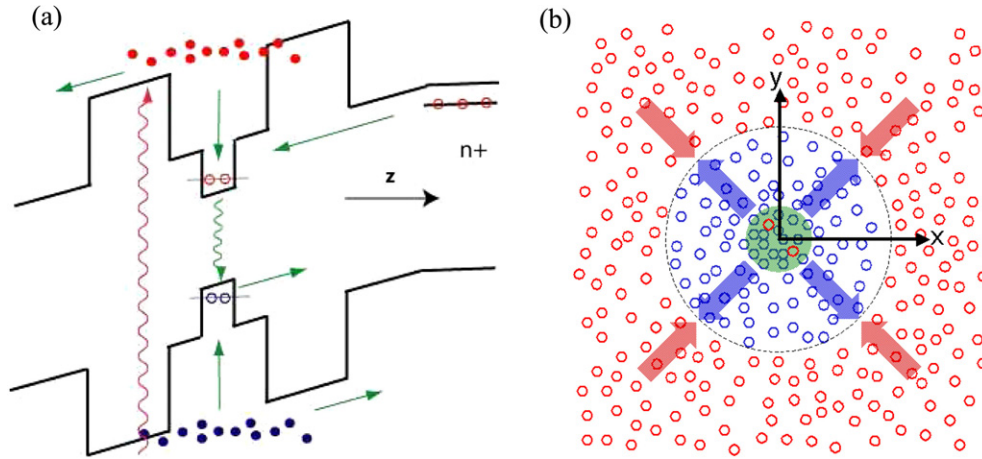
Figure 24. (a) The energy profile of the QW structure in the growth direction and the relevant electronic processes under photoexcitation. (b) Schematic description of in-plane distributions of electrons (open red circles) and excess holes (open blue circles) in the QW under steady state. The excitation spot is marked by the shaded circular area. The recombination of electrons and holes or excitons at the boundary gives rise to the ring pattern.

structures. Under the above-barrier optical excitation and applied bias (figure 24(a)), hot electrons and holes are equally generated at the excitation spot but more holes are eventually trapped in the QW. This is due to the larger hole trapping rate (compared to the electrons) as a result of their smaller drift velocity and higher phonon scattering rate. The excess holes trapped in the QW deplete the initial excess electrons (due to modulation doping and a tunnelling dark current) to form a puddle of holes (at the excitation spot) surrounded by a sea of electrons everywhere else in the QW. The boundary expands due to a continuous accumulation of holes and their outward diffusion and in steady state becomes significantly larger than the excitation spot. This is shown in figure 24(b). The emission of light can only occur at the e–h boundary where the excitons are formed, leading to the luminescence ring pattern. The effective lifetime of these charged carriers is now greatly enhanced even for single QW direct exciton transitions which are inherently very fast. This is due to the effective charge separation where carriers can meet and recombine (or become bound neutral excitons) only on the boundary (the ring).

The above picture can be described by the following model which determines the dynamics of the optically excited carriers:

$$\frac{\partial n_{\text{hot}}}{\partial t} = D_{\text{hot}}^{\text{e}} \nabla^2 n_{\text{hot}} - \frac{n_{\text{hot}}}{\tau_{\text{cool}}^{\text{e}}} - \frac{n_{\text{hot}}}{\tau_{\text{drift}}^{\text{e}}} + A f(r) \tag{15}$$

$$\frac{\partial p_{\text{hot}}}{\partial t} = D_{\text{hot}}^{\text{h}} \nabla^2 p_{\text{hot}} - \frac{p_{\text{hot}}}{\tau_{\text{cool}}^{\text{h}}} - \frac{p_{\text{hot}}}{\tau_{\text{drift}}^{\text{h}}} + A f(r) \tag{16}$$

$$\frac{\partial n_{\text{qw}}}{\partial t} = D_{\text{qw}}^{\text{e}} \nabla^2 n_{\text{qw}} + \frac{n_{\text{hot}}}{\tau_{\text{cool}}^{\text{e}}} - \frac{n_{\text{qw}} - n_{\text{eq}}}{\tau_{\text{leak}}^{\text{e}}} - \xi n_{\text{qw}} p_{\text{qw}} \tag{17}$$

$$\frac{\partial p_{\text{qw}}}{\partial t} = D_{\text{qw}}^{\text{h}} \nabla^2 p_{\text{qw}} + \frac{p_{\text{hot}}}{\tau_{\text{cool}}^{\text{h}}} - \frac{p_{\text{qw}}}{\tau_{\text{leak}}^{\text{h}}} - \xi n_{\text{qw}} p_{\text{qw}}. \tag{18}$$

The first two equations describe the evolution of the density distributions of hot electrons $n_{\text{hot}}(\vec{r})$ and hot holes $p_{\text{hot}}(\vec{r})$ optically excited above the barrier. These carriers can either diffuse in the plane, become trapped in the QW (with a timescale of $\tau_{\text{cool}}^{\text{e,h}}$), or simply drift across the sample

to the electrical contacts in the growth direction (with a time scale of $\tau_{\text{drift}}^{\text{e,h}}$). The source for the hot carriers $Af(r)$ is the optical excitation. Here, $f(r)$ is the normalized excitation beam profile and A is the total absorbed photon flux (each absorbed photon generates one electron and one hole). Similarly, the third and fourth equations describe the dynamics of the density distributions of electrons $n_{\text{qw}}(\vec{r})$ and holes $p_{\text{qw}}(\vec{r})$ in the QW. These carriers will diffuse in the QW plane and are replenished from the hot carriers falling into the QW. They leak to or from the contacts with rates $\tau_{\text{leak}}^{\text{e}}$ and $\tau_{\text{leak}}^{\text{h}}$ in a way that tries to bring the densities back to the (equilibrium) densities of the dark state (n_{eq} for electrons, and zero for holes). Pairs of carriers in the QW can also capture each other with an electron–hole capture (or collision time) coefficient ξ. In this case, they either recombine directly and emit photons or, if the total carrier density is small enough to allow for bound exciton states to be formed, there is a good chance that an electron and a hole would be captured to form an exciton. This exciton will then recombine with an exciton radiative lifetime (which would be short for direct excitons in single QW but much longer for dipolar excitons in DQW structures). Note that the thermodynamics of the excitons has been left out for simplicity as it does not play an important role in describing the gross phenomenology of the emission ring.

Further simplification of these equations can be made by neglecting the hot carrier diffusion which is typically much slower than the drifting and cooling processes. This reduces the problem to a set of only two coupled rate equations for only the carriers in the QW:

$$\frac{\partial n_{\text{qw}}}{\partial t} = D_{\text{qw}}^{\text{e}}\nabla^2 n_{\text{qw}} + C_{\text{e}}Af(r) - \frac{n_{\text{qw}} - n_{\text{eq}}}{\tau_{\text{leak}}^{\text{e}}} - \xi\, n_{\text{qw}} p_{\text{qw}} \tag{19}$$

$$\frac{\partial p_{\text{qw}}}{\partial t} = D_{\text{qw}}^{\text{h}}\nabla^2 p_{\text{qw}} + C_{\text{h}}Af(r) - \frac{p_{\text{qw}}}{\tau_{\text{leak}}^{\text{h}}} - \xi n_{\text{qw}} p_{\text{qw}}. \tag{20}$$

Here, $n_{\text{hot}}/\tau_{\text{cool}}^{\text{e}} = C_{\text{e}}Af(r)$ and $p_{\text{hot}}/\tau_{\text{cool}}^{\text{h}} = C_{\text{h}}Af(r)$ with $C_{\text{e(h)}} = 1/(1 + \tau_{\text{cool}}^{\text{e(h)}}/\tau_{\text{drift}}^{\text{e(h)}})$. $C_{\text{e(h)}}$ can be estimated by comparing the experimentally measured light induced electric current to the number of photogenerated hot carriers. In our simulation, we use $C_{\text{e}} \cong 0.2$ and $C_{\text{h}} \cong 1$. We use a Gaussian beam profile ($f(r)$) to describe our excitation spot with a beam diameter of 60 μm FWHM. The electron diffusion coefficient of $D_{\text{qw}}^{\text{e}} = 20$ μm^2 ns^{-1} is derived from the measured electron mobility. The hole diffusion coefficient is then inferred to be $D_{\text{qw}}^{\text{h}} = D_{\text{qw}}^{\text{e}} m_{\text{e}}/m_{\text{h}} = 5$ μm^2 ns^{-1}. The leakage time τ_{leak} is taken to be on the order of 10 μs, and $n_{\text{eq}} = 10^{11}$ cm^{-2}. ξ, the capture coefficient, is estimated by a simple, classical free electron–hole Coulomb capture model. In this model, a charged carrier is assumed to be captured by an opposite charge if its thermal kinetic energy is smaller than the Coulomb attraction. This model results in a capture cross-section of $\sigma = (\frac{e^2}{6\pi\epsilon kT})^2$. ξ is then given by $\sigma v_{\text{th}}/w = \frac{e^4}{36\pi\epsilon^2 w}\sqrt{\frac{3}{\mu^* k^3 T^3}}$ where v_{th} is the thermal velocity of the carrier, μ^* is the reduced electron–hole effective mass, and w is the thickness of the QW. At a carrier density of 10^{11}, the electron–hole pair capture time is $\sim$1 ns. This number is typically much longer than the recombination time of a direct exciton, $\tau_{X_{\text{D}}}$, in single QW structures but shorter than a typical dipolar exciton lifetime, τ_X, in DQW structures.

The numerical solutions of the model in steady state are presented in figure 25 (under certain simplified assumptions, analytical solutions can be obtained [38]). The laser intensity profile is shown by the dark dotted line. The electron and hole density distribution profiles (solid and dashed lines) clearly show the separation of these opposite charges, depicting a picture where the excess holes in the centre are surrounded by an electron sea with the hole-rich region (or electron depletion region) much larger than the excitation spot. The emission profile (proportional to $n \times p$) shown by the thick grey line portrays the resulting photoluminescence pattern which consists of the centre spot and the ring at the charge separation boundary.

29
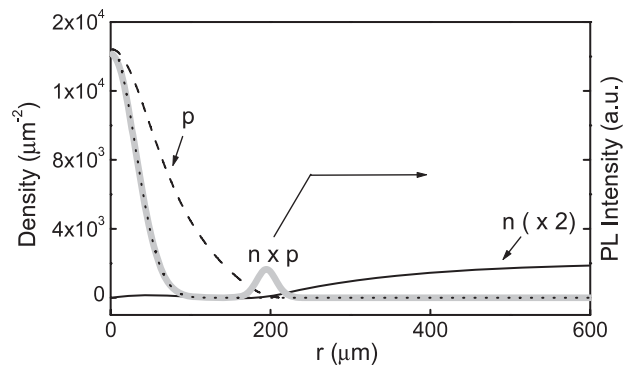
Figure 25. Calculated QW electron (solid line) and hole (dashed line) density profiles and the emission intensity (thick grey line) profile for a CW excitation at a power of 350 μW. The black dotted line shows the incident photon intensity radial profile assuming that $\xi n_{qw} p_{qw} \ll n_X/\tau_X$.
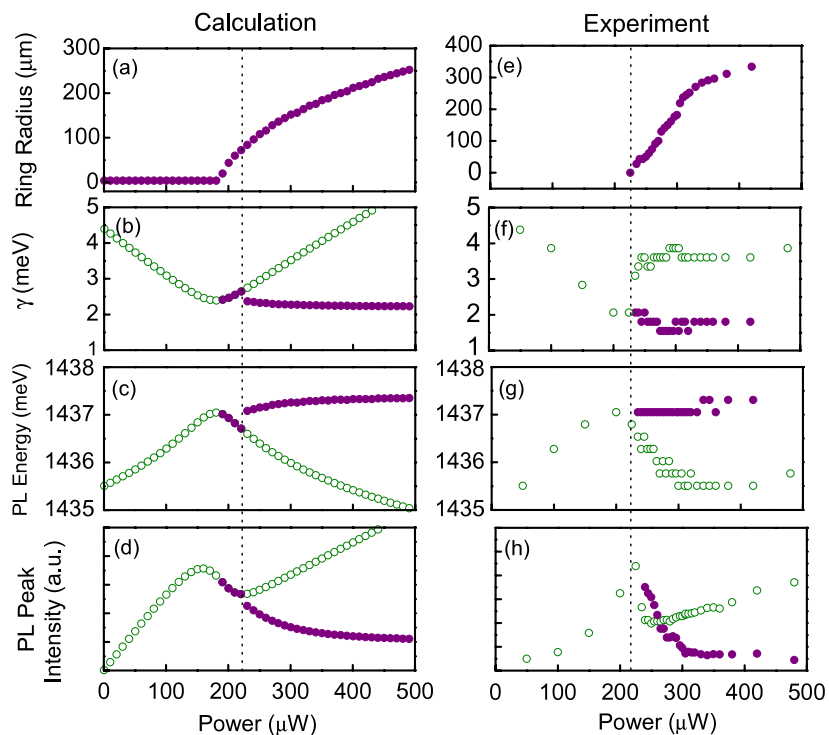
Figure 26. Left panel: calculated centre spot and ring emission spectroscopic characteristics: (a) ring radius, (b) linewidth, (c) energy, (d) intensity, as a function of the excitation power. The open circle and solid dots correspond to the centre spot and the ring emission, respectively. The right panel (e)–(h) is the corresponding experimental results.

This model also allows us to calculate the spectroscopic features of the centre spot and ring emission. For a later comparison with the experimental results, we have particularly calculated the ring radius, the emission linewidth, energy, and intensity of the centre spot and ring emission as a function of the excitation power, shown in the left panel of figure 26. The calculation shows that at low excitation power, the emission only occurs at the excitation spot since the holes that
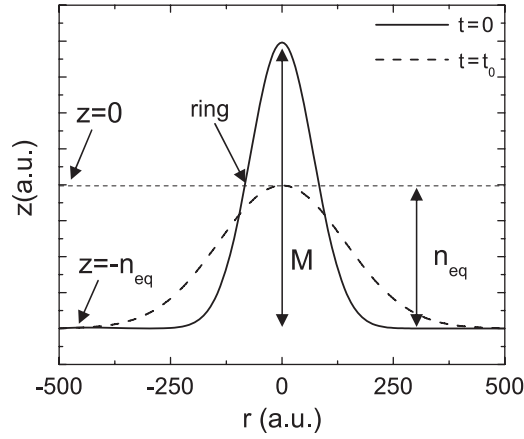
Figure 27. Profiles of z at $t = 0$ and $t = t_0$. The optical excitation at the centre spot is turned off at $t = 0$. The ring appears where $z = 0$. The ring radius shrinks with time and at t_0 it completely collapses.

are captured in the well are not dense enough to deplete the modulation doped excess electrons and thus there is no charge separation. In addition, since the excess electron density is high at the centre, the emission spectrum is broad (figure 26(b)) and red-shifted (figure 26(c)). Here, we assume a quasi-degenerate 2D electron–hole gas, with a emission linewidth determined by the calculated electron and hole densities $\gamma = E_f^e + E_f^h = \pi\hbar^2(n_{qw}/m_e + p_{qw}/m_h)$, in which E_f^e and E_f^h are the electron and hole Fermi energies, and m_e and m_h are the effective masses. The energy shift is due to bandgap renormalization $E_{BGR} = E_0 - \eta(n_{qw}/m_e + p_{qw}/m_h)^{1/3}$ ([39, 40]), with η being a fitting parameter (to experiments). As the excitation power increases, the electrons are gradually depleted at the centre spot, leading to narrower linewidth and smaller red-shift, until the electrons are completely depleted and the charge separation and the ring pattern start to appear (figure 26). As the excitation power is further increased, the boundary of the charge separation expands outward leading to larger ring radii. In the meanwhile, the centre spot becomes hole rich with increasing density, again leading to broader linewidth and larger red-shift. The ring emission, however, remains narrow and little red-shifted, corresponding to relatively low carrier densities at the charge separation boundary (see figure 25 for the electron and hole density profiles).

A very intriguing additional prediction of the model is that the macroscopic charge separation and therefore the ring emission persist for an extremely long time compared to the centre spot lifetime after the laser excitation is turned off [35, 41]. This can be nicely seen analytically with only few simplifications in the above model [41]: the calculation of the ring emission lifetime is performed by combining equations (19) and (20) with the assumption $D_{qw}^e = D_{qw}^h = D^{eh}$ and $\tau_{leak}^e = \tau_{leak}^h = \tau$ to obtain the equation for the charge imbalance $z(r) = p_{qw}(r) - n_{qw}(r)$ with the dark charge imbalance being $z_0 = -n_{eq}$:

$$\frac{\partial z}{\partial t} = D^{eh}\nabla^2 z - \frac{z - z_0}{\tau} + f_z. \tag{21}$$

Here, $f_z = (C_h - C_e)Af(r)$ is the source for the charge imbalance due to the excited carriers falling into the QW. We assume that a steady state charge separation is established by a CW excitation at time zero that can be approximated by a Gaussian function $z(r, t = 0) = Me^{-\frac{r^2}{\Delta^2}} - n_{eq}$, where M and Δ is the excited stationary peak value and width of z. This initial charge imbalance is shown by the solid line in figure 27. The radius of the emission ring at
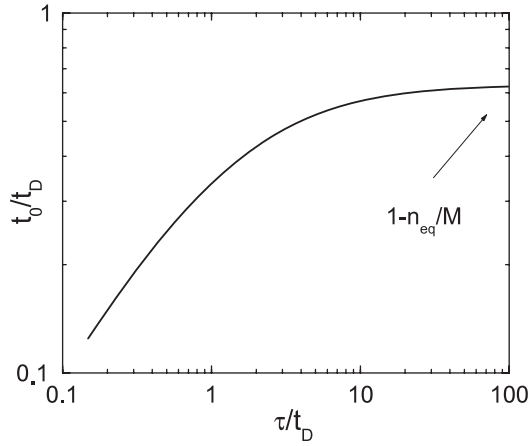
Figure 28. t_0 as a function of the tunnelling time τ in units of the characteristic diffusion time t_D. t_0 is upper bounded by $t_D(1 - n_{eq}/M)$ for large τ and decreases with decreasing τ.

any given time $r_{ring}(t)$ is determined by the condition $z(r_{ring}, t) = 0$, which gives the position of the charge separation boundary ($n_{qw}(r_{ring}) = p_{qw}(r_{ring})$), and its value at $t = 0$ is marked in the figure. The excitation source is then abruptly turned off. The charge imbalance value decreases with time due to the combined effect of charge diffusion and leakage. After some time t_0, the ring radius shrinks to zero, $r_{ring} = 0$, shown by the dashed curve in figure 27. This is when the emission ring disappears into the centre spot. We define this time t_0 as the charge separation response time (or lifetime) and it can be calculated analytically using equation (21) (details are given in [41]). The calculated t_0 is shown in figure 28 as a function of the leakage (tunnelling) time in units of a characteristic diffusion time $t_D = M\Delta^2/4D^{eh}n_{eq}$. We see that the ring response is determined by both the diffusion time t_D and the tunnelling time τ. In particular, it shows that t_0 is upper bounded by $t_D(1 - n_{eq}/M)$ for large τ. As τ becomes shorter, t_0 decreases and is eventually determined by τ for $\tau \ll t_D$. Note that $M - n_{eq}$ is the amplitude of the initial charge imbalance. It is obvious that $M > n_{eq}$ (complete electron depletion at the excitation spot) is a necessary condition for the ring formation and a non-zero t_0.

A steady state peak carrier imbalance density M (2×10^{12} cm^{-2}) and a width Δ (300 μm) can be estimated from experiments [35]. The diffusion time t_D is then calculated to be 250 μs for a hole diffusion coefficient of 2 μm^2 ns^{-1}. Assuming that the tunnelling time is much larger than t_D, t_0 is then $\sim t_D(1 - n_{eq}/M) \sim 200$ μs. This response time is extremely slow as it is much longer than the exciton lifetime.

An important implication of the extremely long response time is that after the excess holes are generated at the excitation spot, they spend hundreds of microseconds migrating to where the emission ring is. Therefore, it is expected that these initially hot holes generated optically in the QW should have enough time to thermalize to the lattice temperature. As a result, the excitons formed at the ring should have an excess kinetic energy due to the electron–hole capture process that is no more than the exciton binding energy (which however might still hinder a complete exciton cooling). In addition, the supply of the excitons at the ring is extremely persistent: the positive and negative charge plasmas remain separated with excitons formed at their boundary for microseconds even if the optical excitation source is turned off.

We note that the above model for the ring formation can be extended to include the effect of the screened Coulomb pressure [42]. This would result in drift terms for the electrons and holes
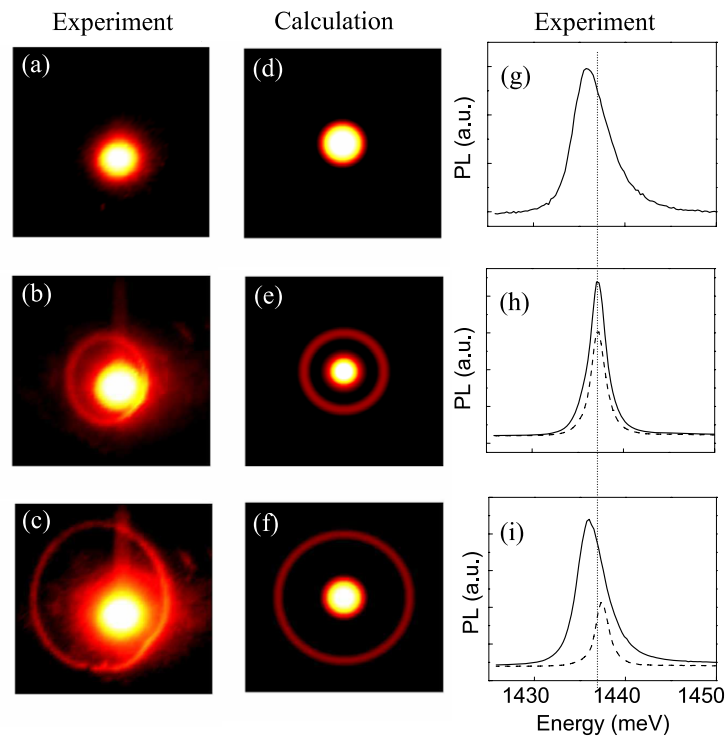
Figure 29. Photoluminescence images for our single QW sample taken at three different excitation powers, 50, 265 and 296 μW, are shown in the left panel (a)–(c). The middle panel (d)–(f) shows the results of the model calculations. The asymmetry of the ring pattern with respect to the centre spot is probably due to a gradient of the barrier width, which is not taken into account in our model. The right panel (g)–(i) presents the corresponding experimentally observed centre spot (solid line) and ring (dashed line) emission spectra. The sample was measured at $T = 8$ K, and excited with a He–Ne laser with a spot diameter of ∼60 μm.

besides the diffusion terms already given in equations (19) and (20). It can also be extended to include the effect of excitation below the barrier energy which tends to decrease the charge imbalance and thus the ring size [43]. We also note that an equation similar to equation (21) was elegantly used in [36] to analytically predict the shape of two converging rings.

7.2. Experimental results

We carried out extensive experiments in a single QW structure with all the results confirming the validity of the model discussed above. Our single QW sample shown schematically in figure 23 consists of a 60 Å $In_{0.13}Ga_{0.87}As$ QW surrounded by GaAs/$Al_{0.32}Ga_{0.68}As$ 50/1000 Å barriers. A 1000 Å layer of Si doped GaAs is located 2000 Å from the QW on the n^+ substrate side and another similar layer is located 1000 Å from the QW on the top contact side. Gold films are deposited on both sides of the sample to form contacts. A 3 mm hole is opened on the top gold film for the optical measurements.

In figure 29, we show the ring emission patterns and spectra at three different powers. The spectra confirm that the centre emission is broad and red-shifted for low and high excitation powers but narrower at the onset of the ring formation. In addition, the centre emission line is slightly asymmetric for low and high excitation powers, characteristic of high carrier
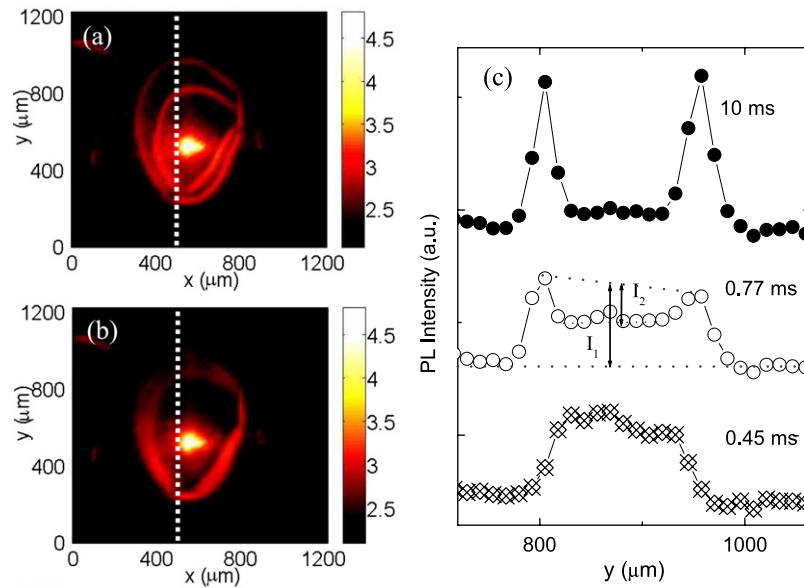
Figure 30. PL images for light intensity modulation experiments at a modulation period of (a) 10 and (b) 0.33 ms (0.1 and 3 kHz). (c) Emission profile along the dashed line in (a) and (b) for various modulation periods, showing the transition from two concentric rings to an annulus. The schematics in the middle curve of (c) show how the ring contrast, $C = \frac{I_2}{I_1}$, is defined.

densities. However, the ring emission, as predicted, remains narrow and symmetric at all powers and resembles a typical excitonic transition lineshape. The power dependence of the various spectroscopic parameters are plotted in the right panel of figure 26, showing excellent agreement with the calculations.

To confirm the prediction that the charge separation is a slow process determined by the carrier diffusion and tunnelling, we use the following method to measure the dynamics (the response time, t_0) of the carriers [41]. The idea is that when an experimental condition, the excitation power for example, is abruptly varied between two values, the ring pattern corresponding to one power will undergo a dynamic change to the pattern corresponding the other with a speed determined by the carrier diffusion and tunnelling, as discussed in the modelling section. If the power alternation (frequency of modulation) is much slower than those processes, a time averaged imaging of the emission will show two distinct rings. However, as the modulation speed is increased to a level that is comparable or faster than the carrier dynamics, the two emission rings will smoothly merge into an annulus. By studying the smoothing of the annulus as a function of the modulation frequency, one can estimate the carrier response time t_0 experimentally.

Figures 30(a) and (b) show such measurements. The excitation power is sharply and square modulated between 900 and 800 μW. The modulation period T is 10 and 0.33 ms for figures 30(a) and (b), respectively. Figure 30(c) plots the cross-section along the dashed line in figures 30(a) and (b) for several modulation periods, showing the smooth transition from two distinct concentric rings to an annulus. We define the contrast of the concentric ring relative to the annulus in between as $C = \frac{I_2}{I_1}$, where I_1 is the *average* peak emission intensity of the two rings, and I_2 is the difference between I_1 and the emission intensity of the plateau *midway* between the rings, respectively illustrated in figure 30(c). In [41] we show that the ring response
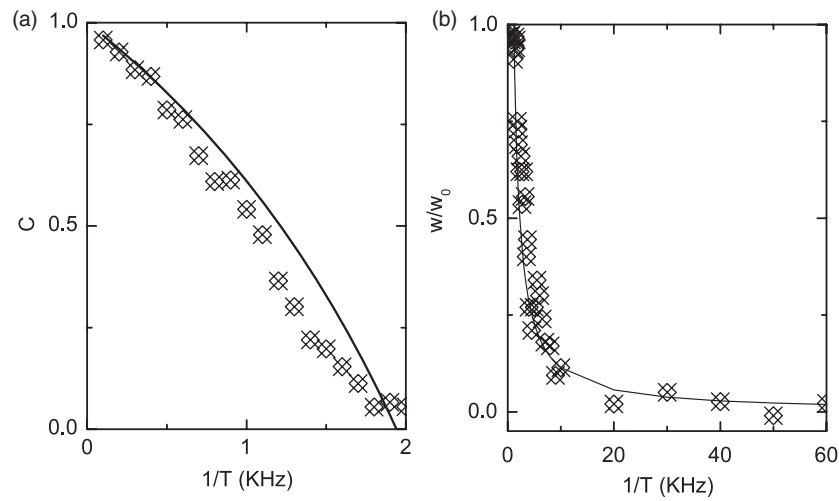
Figure 31. (a) Contrast C of the two emission rings relative to the annulus as a function of the modulation frequency. The solid line is a fit using $C = (T/2 - t_0)/(T/2 - t_0 + At_0)$, where the ring response time t_0 is the only fitting parameter. (b) Normalized annulus width W as a function of modulation frequency. The solid line is the model calculation.

time t_0 is related to C, for all $T \geqslant 2t_0$, through the following expression: $C = \frac{T/2 - t_0}{T/2 - t_0 + 2At_0}$. Here A is the ratio of the ring spatial width and the width of the annulus. Figure 31(a) presents a fit of the above expression to the experimental values of C as a function of $1/T$ from which a value for the ring response time $t_0 = 250\ \mu$s, was obtained.

The other measurable parameter is the width of the annulus, W, which narrows as the modulation speed is increased further since the carriers do not have enough time to respond. Again, we have shown in [41] that W is related to t_0 through the expression $W = W_0 \frac{T}{2t_0}$, where W_0 is the radial distance between the two rings at low modulation frequencies. Figure 31(b) presents W/W_0 as a function of $1/T$ from the experiment and a solid line plotting the theoretical prediction for W/W_0 with $t_0 = 250\ \mu$s, confirming the previous extracted value for the response time. This very large value is consistent with the model result discussed previously. It is important to note that the above experiments were also performed under different excitation intensity modulation depth. We found that the ring response time does not vary much even for modulations in which the lower intensity is almost zero and the charge boundary moves all the way between the excitation spot and a large diameter ring (the situation that the model calculation was based on in the section 7.1). These observations are also consistent with numerical calculations.

7.3. Exciton rings as a source of dipolar excitons

After we have established the model for the origin of the exciton emission ring and the understanding of the ring dynamics and the timescales associated with it, we would like to have a short discussion of the ring as a source of dipolar excitons and the simple way to incorporate it into the model that we have used to analyse dipolar exciton dynamics in either the free expansion case and the electrostatic trapping case.

As we have mentioned before, the model for the charge separation developed in section 7.1 can give the spatial distribution of both the electrons ($n_{\text{qw}}(r, t)$) and holes ($p_{\text{qw}}(r, t)$) in the planes of the DQW. The rate of e–h capture that leads to the creation of excitons was given by

$\xi n_{qw} p_{qw}$ in equations (19) and (20). Going back to the exciton model presented in section 4, this e–h capture rate can be used as the source for dipolar excitons in equation (6), by setting $I_X(r, t) = \xi n_{qw} p_{qw}$ for any r where n_{qw}, $p_{qw} < n_{mott}$, with n_{mott} being the transition density to e–h plasma. Such a connection between the two previously independent models can be done by assuming that with the above condition on the densities, we can neglect the process in which opposite charge carriers recombine without first creating an exciton and that the formation of excitons does not significantly affect the charge separation dynamics. In this case, equation (6) takes the form:

$$\frac{\partial n_X}{\partial t} + \nabla \cdot (\mathbf{J}_D + \mathbf{J}_d) + \frac{n_X}{\tau_X} - \xi n_{qw} p_{qw} = 0, \tag{22}$$

where n_{qw}, p_{qw} are independently obtained from equations (19) and (20), and ξ can either be calculated from the model presented in section 7.1 or can be tuned as a free parameter. We also note that for a DQW ring system, τ_X, is now the effective exciton lifetime on the ring, and is expected to be significantly shorter than its intrinsic recombination lifetime. This is due to the fact that one expects a strong in-plane radial field in the ring, due to the effect of the charge separation between the inner and outer sides of the ring radius. These in-plane fields will tend to break the excitons at the two boundaries of the ring, in a manner similar to the effect on the electrostatic trap boundary, thus giving rise to an effective exciton lifetime that can become very short.

8. Exciton cooling—experimental considerations

In the previous sections, we described three possible techniques used for obtaining cold dipolar excitons at high densities, i.e., free expanding excitons, excitons trapped in electrostatic traps and excitons formed in rings. In this section we would like to point out some practical issues of the cooling of excitons and present some simple guidelines for the experimental requirements. In particular, we want to refer to the effect of heating from the excitation source, under different experimental conditions, and to present simple 'rule of thumb' approximations for its importance in the experiments.

We have shown that under pulsed excitation, the driven expansion of the dipolar fluid leads to a fast reduction of the fluid density as well as an effective heating that slows down the exciton cooling to the lattice temperature. Considering the case of CW excitation, the fluid will eventually reach a steady state, both in its density profile and its temperature. Under such steady state conditions, a continuous excitation of hot excitons is needed in order to replenish the exciton population which is being constantly depleted via recombination. These excitons carry excess kinetic energy due to the difference in their excitation energy with respect to the cold dipolar excitons (under a typical non-resonant excitation).

To estimate the effect of heating due to the excess energy of the excited hot excitons, we assume that excitons are created by the laser, each with an excess energy $\Delta\varepsilon_{X0}$ (and thus carries an effective excess temperature $\Delta T_{X0} = \Delta\varepsilon_{X0}/k$). As exciton–exciton scattering is very efficient, this excess heat will be quickly distributed between the rest of the excitons. In steady state, the total flow of excitons from the source (which is found by setting time derivatives to zero in equation (6) and integrating it over space), $I_X^t = \int I_X(r)\, d^2r$, is given by

$$I_X^t = N_X^t / \tau_X, \tag{23}$$

where $N_X^t = \int n_X(r)\, d^2r$ is the total number of excitons. The flow of heat into the system per exciton, assuming instantaneous and equal distribution between all excitons, is then

$$I_T = \Delta T_{X0} I_X^t / N_X^t = \Delta T_{X0} / \tau_X. \tag{24}$$

Setting equation (24) into equation (7) in steady state yields:

$$\Delta T_X = I_T \tau_1 = \Delta T_{X0} \frac{\tau_1}{\tau_X}, \tag{25}$$

where $\Delta T_X \equiv T_X - T_1$, is the heating due to the CW hot exciton source in steady state. This heating term is density independent and only depends on the excess temperature of the excitons coming from the source and the ratio of the cooling time to the exciton lifetime. For typical experimental values of laser excitation into the direct excitons, $\Delta E_{X0} = E_{\text{direct}} - E_X \cong 25$ meV and thus $\Delta T_{X0} = 300$ K, we get $\Delta T_X(\text{K}) \approx 300\tau_1/\tau_X$, and it is clear that under such circumstances, it is preferable to have very long lifetime excitons to minimize exciton leakage and thus the heating. To be a little more specific, we can require that the excitons be highly degenerate, i.e., $T_0/T_X = T_0/(T_1 + \Delta T_X) \gg 1$. Setting $T_1 = 1$ K and $T_0 = 4$ K for $n_X \simeq 6 \times 10^{10}$ cm^{-2} for typical experiments of dipolar excitons described above, we get $\Delta T_X < 3$ K and thus $\tau_X \gg 100\tau_1$. The exact value of τ_1 is hard to determined, and as far as we know, there are no conclusive measurements of it in dipolar exciton systems similar to the ones described in this paper. If this number is of the order of nanoseconds, as was calculated theoretically [15], it requires exciton lifetimes of the order of microseconds.

Equation (25) holds for excitons in electrostatic traps and in rings for the CW excitation. In the case of excitons trapped in electrostatic traps, one have to replace the exciton lifetime τ_X with the effective trap lifetime τ_{trap}. For high quality traps, these two are essentially the same. Therefore, cooling and steady state temperature of free expanding excitons and trapped excitons are similar for the CW case, in contrast to the pulsed excitation experiments described in previous sections in which the dipole heating leads to slower cooling for the free expanding excitons. One has to remember however, that there is still a strong expansion of excitons without a trap. This means that to achieve high exciton densities without trapping, much higher pump powers are necessary, which could lead to a significant residual absorption of light by the lattice which can then cause a heating of the lattice itself. Furthermore, CW experiments in general pose a much more strict requirement on the exciton lifetime due to the residual heat source compared to the pulsed excitation experiments. As seen above, in the CW case, τ_X has to be orders of magnitude longer than τ_1, while in the pulsed excitation experiment, the dipolar excitons in a trap (but not free expanding) are expected to cool to the lattice temperature after a time that correspond to only few cooling times τ_1, which relaxes the requirement on τ_X.

As for exciton rings, since the charged carriers thermalize as they approach the ring, ΔT_{X0} is expected to be significantly smaller, while as we have mentioned before, the effective exciton lifetime on the ring might also be significantly shorter than its intrinsic recombination lifetime. It is hard to get more than a rough estimate of the combined effect of the carrier thermalization and the effective ring lifetime without intensive calculations or a proper measurement. In a recent paper [37], the exciton lifetime on the ring was quoted to be 40 ns, however no explanation was given on how this lifetime was extracted. It is not clear, but certainly possible, that excitons on the ring are indeed cold enough to become degenerate at high densities, and recent intriguing results may suggest effects related to such degeneracy [37, 44]. Again, in all cases, caution has to be taken when considering the above issues, and an independent measure of the exciton lifetime and temperature would be extremely beneficial.

9. A note about trapped dipolar excitons crystal phase

It is interesting to note that exciton traps such as the ones described in details in section 6 form a sharp boundary for the dipolar excitons, and essentially confine them in a small 'bucket'. In such case, excitons with a net repulsive interaction can in principle reach high density

equilibrium and form a crystal phase. This phase, if stable, can compete with other quantum phase transitions such as, for example, to a superfluid state.

To try to estimate the stability of such a crystal phase, we first calculate the total energy of a 2D lattice of classical dipoles, aligned perpendicular to the 2D plane and arranged, for example, in a square lattice formation (this may not be the lowest energy stoichiometry, but it will suffice for the rough estimate we are after). The total potential energy of such a crystal in equilibrium is given by:

$$\varepsilon_d^p = \sum_{\substack{n,m=-\infty \\ |n|+|m|\neq 0}}^{\infty} \frac{d^2}{\epsilon r_0^3} \frac{1}{(n^2+m^2)^{3/2}} \simeq \frac{12d^2}{\epsilon r_0^3} = \frac{12d^2}{\epsilon} n_X^{3/2}, \tag{26}$$

where r_0 is the lattice constant. Next, the harmonic approximation for small vibrations around equilibrium yields

$$\omega_0^2 \simeq \frac{18d^2}{\epsilon m_X r_0^5} = \frac{18d^2}{\epsilon m_X} n_X^{5/2}. \tag{27}$$

For a given vibrational mode of the dipolar crystal, $\omega_s(\vec{k})$, the amplitude of the zero point motion is given, using the virial theorem, by $\langle U_s^2(\vec{k})\rangle = \langle \varepsilon_{zpm}(s,\vec{k})/K(s,\vec{k})\rangle$, where $K(s,\vec{k}) = m_X\omega_s^2(\vec{k})$. Since due to symmetry, $\langle(\Delta U)^2\rangle_{zpm} = (\langle U^2\rangle_{zpm} - \langle U\rangle_{zpm}^2) = \langle U^2\rangle_{zpm}$, the total amplitude of the zero point motion can then be estimated from the sum:

$$\langle(\Delta U)^2\rangle_{zpm} = \frac{1}{n_X}\sum_{\vec{k},s}\frac{1}{2}\hbar\omega_s(\vec{k})/(m_X\omega_s^2(\vec{k})) = \frac{1}{n_X}\sum_{\vec{k},s}\frac{\hbar}{2m_X\omega_s^2(\vec{k})}. \tag{28}$$

Taking a simple dispersion form of a monatomic crystal and considering only the acoustic modes, this sum can be integrated with the result,

$$\langle(\Delta U)^2\rangle_{zpm} \approx \frac{\hbar}{2m_X\omega_0}. \tag{29}$$

Applying the Lindemann criterion for melting $\langle(\Delta U)^2\rangle = C_1^2 r_0^2$, we get

$$\left(\frac{2\hbar^2\epsilon}{9m_X}\right)^{1/2}\left(\frac{1}{n_X^{melt}}\right)^{1/4} \approx C_1^2. \tag{30}$$

If we (quite arbitrarily) choose a Lindemann parameter with a typical number $C_1 \sim 0.2$ and insert dipolar exciton parameters typical to our GaAs system, we get a melting density $n_X^{melt} \approx 1 \times 10^{15}$ cm^{-2}, which indicates that a dipolar exciton crystal would not be stable due to the zero point motion for all densities below the transition density to e–h plasma ($n_{mott} \sim 1 \times 10^{11}$ cm^{-2}), which is also a typical density range where the dipolar approximation is still valid in similar systems. Thus the crystal, at least in its simple form, would not compete with other phase transitions of the exciton fluid at low temperatures and high densities. It is interesting that this very crude approximation is within the same order of magnitude of the result of a recent Monte Carlo calculation of the melting transition of a 2D dipolar crystal by Astrakharchik *et al* [45] ($n_X^{melt} \approx 7 \times 10^{15}$ cm^{-2} when using same parameters). The above result is not surprising as the dipolar excitons are very light ($m_X \simeq 0.2\ m_e$) and the dipole–dipole interaction is rather weak, leading to a very non-stiff, unstable crystal.

10. Summary

The aim of this paper was to give an overview of the three different experimental configurations (or techniques) that are recently leading the research of cold dipolar excitons in GaAs DQW

heterostructures and which we have been experimenting with for the last few years. These are free exciton fluids, electrostatically trapped excitons and excitons in excitonic rings. The model we have presented seems to account well for most of the experimental results in all these configurations, and allows us to get a deeper insight into their complex dynamics. We have discussed the advantages and disadvantages of each of these configurations with both pulsed and CW excitations. We find that in general, a pulsed excitation has less stringent restrictions on the ratio of the cooling time to the lifetime cooling compared to a CW excitation, due to the absence of a continuous heating source. We also show that under such a pulsed excitation, an in-plane trapping of the dipolar exciton fluid seems to be necessary due to the fast expansion and expansion induced heating of the excitons resulting from their mutual dipole repulsion. We have shown that electrostatic trapping of excitons, with the proper design, seems to well resolve this expansion problem by effectively confining the excitons in a small area. We also presented a model to account for the physical origin of excitonic rings, and showed that it can be considered as a potential CW source for cold excitons, considering its limitations. The effect of heating sources under CW excitation was discussed and 'rule of thumb' requirements from all the above configurations were presented.

With all the above considerations carefully accounted for, it seems that quantum degenerate dipolar exciton fluids are within reach, and with the dynamics of the excitons in those systems now fairly clear, unambiguous experimental evidences for quantum degeneracy and possibly phase transitions of such excitons are now needed. We want to finally note that such efforts are indeed ongoing, both in our group as well as in others. Some very recent results are especially intriguing, and may be related to exciton degeneracy or exciton correlations. To mention just some, the origin of the excitonic 'beading' is still unclear [33, 36, 46], and recent measurements claim that these beads display an extended spatial coherence [37] which is absent at higher temperatures. Similar pattern formation was also detected in other ring-like systems [44, 47, 48], where again evidence of temperature dependent coherence was observed. In our group, we have recently measured the correlations between the exciton excess internal energy and their density, as the density decays with time. The interpretation of all the above results have to be done with an extreme caution, as these systems are notoriously complex, but they at least indicate that there are a lot of novel effects of cold dipolar excitons that need to be properly explained.

Acknowledgments

References

[1] Keldysh L V and Kozlov A N 1968 *JETP* **27** 521
[2] Anglin J R and Ketterle W 2002 *Nature* **416** 211
[3] Kosterlitz J M and Thouless D J 1973 *J. Phys. C: Solid State Phys.* **6** 1181
[4] Lozovik Y E and Yudson V I 1975 *JETP Lett.* **22** 274
[5] Fernandez-Rossier J and Tejedor C 1997 *Phys. Rev. Lett.* **78** 4809
[6] Butov L V 2004 *J. Phys.: Condens. Matter* **16** R1577
[7] Snoke D 2002 *Science* **298** 1368
[8] Fukuzawa T, Mendez E E and Hong J M 1990 *Phys. Rev. Lett.* **64** 3066

[9] Alexandrou A, Kash J A, Mendez E E, Zachau M and Hong J M 1990 *Phys. Rev.* B **42** R9225
[10] Tan M Y J, Drummond N D and Needs R J 2005 *Phys. Rev.* B **71** 033303
[11] Szymanska M H and Littlewood P B 2003 *Phys. Rev.* B **67** 193305
[12] Ivanov A 2002 *Europhys. Lett.* **59** 586
[13] Rapaport R, Chen G and Simon S 2006 *Phys. Rev.* B **73** 033319
[14] Rapaport R, Chen G and Simon S H 2006 *Appl. Phys. Lett.* **89** 152118
[15] Ivanov A, Littlewood P and Haug H 1999 *Phys. Rev.* B **59** 5032
[16] de Leon S B-T and Laikhtman B 2001 *Phys. Rev.* B **63** 125306
[17] Voros Z, Balili R, Snoke D, Pfeiffer L N and West K 2005 *Phys. Rev. Lett.* **94** 226401
[18] Ivanov A L, Smallwood L E, Hammack A T, Yang S, Butov L V and Gossard A C 2006 *Europhys. Lett.* **73** 920
[19] Sakaki H, Noda T, Hirakawa K, Tanaka M and Matsusue T 1987 *Appl. Phys. Lett.* **51** 1934
[20] Prange R and Nee T W 1968 *Phys. Rev.* **168** 779
[21] Gold A 1986 *Solid State Commun.* **60** 531
[22] Gold A 1987 *Phys. Rev.* B **35** 723
[23] Snoke D, Liu Y, Voros Z, Pfeiffer L N and West K 2005 *Solid State Commun.* **134** 37
[24] Hammack A T, Griswold M, Butov L V, Smallwood L E, Ivanov A L and Gossard A C 2006 *Phys. Rev. Lett.* **96** 227402
[25] Zimmermann S, Govorov A O, Hansen W, Kotthaus J P, Bichler M and Wegscheider W 1997 *Phys. Rev.* B **56** 13414
[26] Govorov A O and Hansen W 1998 *Phys. Rev.* B **58** 12980
[27] Zimmermann S, Schedelbeck G, Govorov A O, Wixforth A, Kotthaus J P, Bichler M, Wegscheider W and Abstreiter G 1998 *Appl. Phys. Lett.* **73** 154
[28] Gorbunov A V and Timofeev V B 2004 *JETP Lett.* **80** 210
[29] Hammack A T, Gippius N A, Andreev G O, Butov L V, Hanson M and Gossard A C 2006 *J. Appl. Phys.* **99** 066104
[30] Rapaport R, Chen G, Simon S, Mitrofanov O, Pfeiffer L N and Platzman P M 2005 *Phys. Rev.* B **72** 075428
[31] Miller D A B, Chemla D S, Damen T C, Gossard A C, Wiegmann W, Wook T H and Burrus C A 1985 *Phys. Rev.* B **32** 1043
[32] Chen G, Rapaport R, Pfeiffer L N, West K, Platzman P M, Simon S H, Voros Z and Snoke D 2006 *Phys. Rev.* B **74** 045309
[33] Butov L V, Gossard A C and Chemla D S 2002 *Nature* **418** 751
[34] Snoke D, Denev S, Liu Y, Pfeiffer L and West K 2002 *Nature* **418** 754
[35] Rapaport R, Chen G, Snoke D, Simon S H, Pfeiffer L, West K, Liu Y and Denev S 2004 *Phys. Rev. Lett.* **92** 117405
[36] Butov L V, Levitov L S, Mintsev A V, Simons B D, Gossard A C and Chemla D S 2004 *Phys. Rev. Lett.* **92** 117404
[37] Yang S, Hammack A T, Fogler M M and Butov L V 2007 *Phys. Rev. Lett.* **97** 187402
[38] Haque M 2006 *Phys. Rev.* E **73** 066207
[39] Tränkle G, Lach E, Forchel A and Scholz F 1987 *Phys. Rev.* B **36** 6712
[40] Schmitt-Rink S, Ell C, Koch S W, Schmidt H E and Haug H 1984 *Solid State Commun.* **52** 123
[41] Chen G, Rapaport R, Simon S H, Pfeiffer L N and West K 2005 *Phys. Rev.* B **71** 041301(R)
[42] Snoke D, Denev S, Liu Y, Simon S, Rapaport R, Chen G, Pfeiffer L and West K 2004 *J. Phys.: Condens. Matter* **16** S3621
[43] Rapaport R, Chen G, Snoke D, Simon S H, Pfeiffer L, West K, Liu Y and Devev S 2004 *Phys. Status Solidi* a **201** 655
[44] Gorbunov A V and Timofeev V B 2006 *JETP Lett.* **83** 146
[45] Astrakharchik G E and Boronat J 2007 *Phys. Rev. Lett.* **98** 060405
[46] Levitov L S, Simons B D and Butov L V 2005 *Phys. Rev. Lett.* **94** 176404
[47] Gorbunov A V and Timofeev V B 2006 *JETP Lett.* **84** 390
[48] Keeling J, Levitov L S and Littlewood P B 2004 *Phys. Rev. Lett.* **92** 176402